Inertial effects on deformation and breakup of a two dimensional droplet in simple shear flow

Lyn Wilson

Thesis submitted for the degree of Master of Philosophy

The University of Edinburgh
September 2002

Abstract

Lattice Boltzmann simulations are used to investigate the effect of inertia on droplet breakup in two dimensions. A spherical droplet is placed in a second fluid, with identical properties (i.e. density, viscosity) and subject to a simple shear flow.

The aim is to locate the point beyond which no stable droplet shape exists, and is achieved by implementing a recursive 'velocity ramp' algorithm. When a stationary state is reached the configuration is saved and the shear rate then increased by a given amount. If this has the effect of either causing the drop to break or deform more than a given threshold the previous configuration will be reloaded and the shear increment reduced by half. Otherwise the simulation is continued until another stable shape is reached and the process is repeated. Three dimensionless parameters are used to characterise this process: capillary number, Ca, (ratio of shear stress/surface tension), Reynolds number, Re, (ratio of inertial/viscous terms), deformation, D, (defined to be the ratio of difference/sum of the long and short axis of the drop).

As the viscosity is increased (or Reynolds number decreased) from one run to the next the Re/Ca ratio steadily decreases and the breakup point of the first few runs follows a gradual trend. For these runs at the lower end of the viscosity range simulated, the drops evolve into a two lobed structure orientated at $\sim 60^{\circ}$ to the undisturbed flow lines and break up into two equally sized droplets. Increasing the viscosity further rotates the drops until they are almost aligned with the undisturbed flow lines. Such droplets experience less shear stress and hence withstand greater shear rates. At this point it is found that there is an abrupt change in the morphology of the breaking drop and therefore in plots of Re vs Ca and D vs Ca. The drop now evolves into a three lobed structure, having a large central 'body' with smaller lobes at either end of similar size and shape. Such drops attain deformations of up to ~ 0.9 before breakup. That these shapes are stable is somewhat surprising not only because of their extremely elongated and slender shape but also because the curvature at the ends of the central body would be expected to be unstable due to the Laplace pressure.

Using a slightly modified velocity ramp algorithm, where the restriction on the deformation in response to an increase in shear is lifted, the simulations result in a three lobed mode of breakup for all viscosities. This shows that the details of the flow rate history can strongly affect the outcome.

Several important parameters need careful attention including the mobility and lattice size; these are found to play an important part in the deformation and breakup process. Vortices are also apparent in some morphologies; it is still not certain how these influence or instigate breakup. The limiting case of zero Reynolds number is simulated and results suggest that in this limit there is no hydrodynamic drop breakup in two dimensions.

Declaration

I declare that this thesis has been composed by myself and that the work reported herein has been executed by myself unless otherwise indicated.

Contents

List of Figures

Chapter 1

Introduction

Droplet deformation and breakup under flow is far from a new field of research. In 1833, for example, Savart [18] studied the decay into droplets of a jet of water, then in 1849 Plateau [12] demonstrated that surface tension was the cause of breakup. However, even after many years of study this subject is by no means exhausted and is still providing challenges experimentally, computationally and theoretically. For general reviews see [21], [14].

In this study lattice Boltzmann simulations are used to investigate the effect of inertia on droplet breakup in two dimensions in simple shear flow. Simulation details are given in chapter 3. Two different mechanisms act in achieving droplet breakup: hydrodynamic and diffusive. Inertia may arbitrate as to which one dominates in the breakup process, at least until the breakup point itself [6] (which is thought to be diffusive; in a purely hydrodynamic description breakup requires a singularity of the fluid-fluid interface, however the final disconnection generally involves diffusion).

The system used to study this consists of a circular droplet placed centrally in a second fluid with identical properties (i.e. density, viscosity) and subject to a simple shear flow in two dimensions. This is basically a fully separated binary fluid system in which the minority fluid has assumed its equilibrium configuration – free energy minimisation dictates this to be circular. Free energy minimisation is the driving force of the process of breakup via surface tension. In chapter 2 the background and thermodynamics of the system and problem are described.

Solid walls are introduced to generate the shear flow and the drop has an array of periodic

neighbours. Increasing the shear flow slowly the aim is to locate the point beyond which no stable droplet shape exists.

Similar studies undertaken previously in two ([19], [8]) and three ([16]) dimensions concentrate on varying parameters such as the viscosity difference of the drop to the surrounding fluid and mode of shear used to deform and break the drop i.e. pure extensional flow or pure shear flow. Also, a common method of applying a shear flow to the drop is to suddenly start the shear at the final value and allow the drop to deform and stabilise or carry on and break up. This is one of the main differences between this study and the others; here the shear rate is incremented slowly and at each step the droplet is allowed to deform and reach an equilibrium shape at that shear flow – a velocity ramp algorithm has been implemented to control this process. Another important simulation parameter which is often overlooked is the actual size of the system – the solid walls and the periodic neighbour all influence the breakup. The system used to study this problem as well as details of some other studies in this field are contained in chapter 4. Details of the velocity ramp algorithm are also to be found here.

The coupling of the imposed simple shear flow, the flow generated by the droplet interface (which is shape dependent) and the flow generated due to interactions with the solid walls and periodic neighour make the problem complex and a large parameter space only compounds this. Lattice artifacts are present in the simulation and must be acknowledged and compensated for or corrected. These simulation limitations, choice of parameters and data analysis methods are found in chapter 5.

Inertia plays a fundamental role in the process of droplet breakup; without it in a zero Reynolds number systems a drop will deform until thin enough that the interfaces interact and diffusion ensues. Two morphologies are seen at the point of breakup, one of two lobes and another of three. As the parameters are varied a sharp transition between these two modes of breakup is apparent.

Chapters 6 and 7 contain the results and conclusions, respectively of the study performed here.

Chapter 2

Binary Fluids

2.1 Symmetric Binary Fluids

Symmetric binary fluid systems consist of two species of fluid particles which have identical properties (density, viscosity etc.) but experience a mutual repulsion. As a consequence of a change in temperature such systems will undergo phase separation in order to minimise free energy.

Above a critical temperature, T_c, the two fluids are completely mixed and a disordered phase results with properties indistinguishable from that of a single fluid. However when quenched well below this temperature, due to the mutual repulsion, the system will undergo phase separation: the different components separate out into two distinct, ordered phases. The dynamics and morphology of the ensuing separation process are dependant upon the volume fraction of the fluids: for a 50:50 mix the separation will proceed forming a bicontinuous structure, a network of interlocking domains of similar particles which coarsen with time t_0 reducing interfacial area (see section 2.2) until the system has completely separated into two domains. For unequal volumes in three dimensions this remains the case until the minority phase occupies less than approximately 15-20% of the total volume fraction [20]; in this case droplets will form. Since these have already assumed a spherical structure the free energy can then only be minimised by droplet diffusion and coalescence.

To keep track of the state of the system an order parameter ϕ is defined, which is in general zero in the disordered (high temperature) phase and non-zero in the ordered (low temperature)

phase. In the binary fluid case ϕ is defined to be the density difference between the two fluids ($\phi = \rho_A - \rho_B$) and is, for convenience chosen to take the values ± 1 in each of the respective ordered phases.

2.2 Thermodynamics

Free energy minimisation is the driving force for separation in a binary fluid system.

$$F = E - TS \tag{2.1}$$

where F is the free energy, E the energy, T temperature and S the entropy [3].

For $T > T_c$ thermal motion is dominant and free energy is minimised by maximising entropy, resulting in a stable, completely mixed state, which can be treated as a single fluid. Here the system reaches a global minimum at $\phi = 0$ with the free energy being a concave function of ϕ (see fig 2.1) and hence $\partial F/\partial \phi = 0$ and $\partial^2 F/\partial \phi^2 > 0$. At the critical point $T = T_c$, $\partial F/\partial \phi = 0$, however, $\partial^2 F/\partial \phi^2 = 0$ (see diagram).

When $T < T_c$, however, the repulsive interactions between the fluid particles become dominant and separation occurs. $\phi = 0$ is now an unstable point and the system minimises its free energy by separating into two domains of equilibrium composition. This is reflected in the free energy function which now develops two symmetric minima (see fig 2.1).

Initially phase separation proceeds via a purely diffusive mechanism until well defined domains with sharp interfaces have formed. At this point all excess energy is stored in the interfaces and free energy minimisation now becomes a case of surface area minimisation; two completely separated and coexisting phases being the final equilibrium state.

The free energy of the system is often described by the Landau free energy functional, which, strictly is only valid near the critical point. However for the Lattice Boltzmann algorithm used here any free energy with a double well form suffices to reproduce the correct behaviour of phase separation. Below is an example of a suitable free energy form,

$$F[\phi] = \int \{\nu(\phi) + \frac{\kappa}{2}(\nabla\phi)^2\} dx \tag{2.2}$$

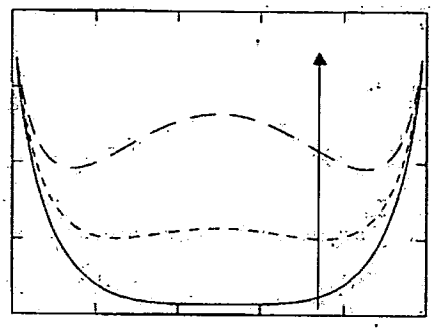

Figure 2.1: representation for free energy $F(\phi)$ for phase separation. Solid line gives critical point; dashed line is phase separated system. The arrow indicates decreasing temperature.

where $\nu(\phi)$ is a potential chosen to have two symmetric minima (see figure 2.2) and the gradient squared term, $(\nabla\phi)^2$, represents the energy stored in the interface.

Immediately after the system is quenched it can be thought of as residing at the point $\phi = 0$, which is clearly unstable to infinitesimal perturbations. For a sufficiently deep quench the system will begin to separate immediately into two phases; the compositions, $\pm\phi^*$, being the equilibrium compositions. (We will choose $|\phi^*| = 1$.)

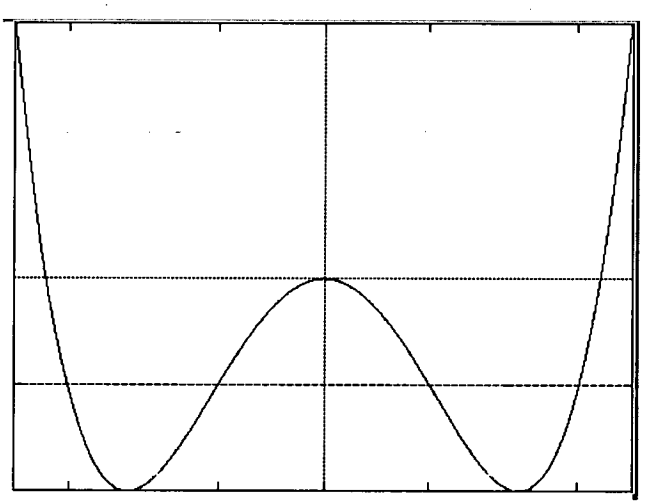

Figure 2.2: symmetric double well potential $\nu(\phi)$

For the simulations under consideration the chosen form of the free energy is one of a ϕ^4 model

$$F[\phi] = \int \{\frac{A}{2}\phi^2 + \frac{B}{4}\phi^4 + \frac{\kappa}{2}(\nabla\phi)^2 + \frac{1}{3}\rho\ln\rho\}dx \tag{2.3}$$

where ρ is the total fluid density. The last term is irrelevant if the fluid remains incompressible (as is assumed here) [5]. The chemical potential is therefore

$$\mu = \delta F[\phi]/\delta\phi = A\phi + B\phi^3 - \kappa\nabla^2\phi \tag{2.4}$$

This particular model free energy, and hence functions derived from it such as the chemical potential (which contain simple powers of ϕ) and the pressure tensor, are computationally less intensive than a model involving, for example logarithmic functions of ϕ. It is also preferred for lattice Boltzmann studies since the free energy is a smooth function, whereas more physically realistic functions will involve steep gradients incurring instabilities when evaluated on a lattice.

The equation describing the time evolution of this conserved order parameter ϕ via diffusive mechanism is

$$\partial\phi/\partial t = M\nabla^2\mu \tag{2.5}$$

In a state of thermal equilibrium

$$\delta F[\phi]/\delta\phi = \mu = constant \tag{2.6}$$

Hence an expression for the interface profile may be derived for a symmetric fluid in equilibium by setting $\mu = constant = 0$, by symmetry and considering a stationary (no hydrodynamics needed) state.

$$\kappa\nabla^2\phi - \partial\nu(\phi)/\partial\phi = 0 \tag{2.7}$$

Introducing a coordinate, g, normal to the interface and setting ϕ to zero at the centre of the interface, integration across the interface gives

$$\kappa/2(\partial\phi/\partial g)^2 = \nu(\phi) - \nu(\phi^\star) \tag{2.8}$$

The interfacial tension σ is just the excess free energy per unit area of the interface and is given by,

$$\sigma = \int \left[\kappa/2(\partial\phi/\partial g)^2 + \nu(\phi) - \nu(\phi^\star)\right] dg \tag{2.9}$$

Integrating through the interface and assuming $\nabla\phi \to 0$ in the bulk fluid ie. sufficiently far from the interface,

$$\sigma = \int_{-\phi^*}^{+\phi^*} (2\kappa)^{1/2} \left[\nu(\phi) - \nu(\phi^*)\right]^{1/2} \partial\phi \tag{2.10}$$

An expression for the interface tension can now be found having selected an appropriate potential.

For the 'ϕ^4' free energy used here (see eq. 2.3) the interfacial equilibrium profile is given by a tanh curve: $\phi/\phi^* = \tanh(g/\xi_0)$, where g is a coordinate normal to the interface and $\xi_0 = (-\kappa/2A)^{1/2}$ provides a measure of the interface width.

Considerations as to selecting the optimum interface width for simulations are given in section 5.1.1.

Thermodynamically for a minority phase binary fluid system spherical droplets will form, minimising surface area and therefore free energy. In such a system free energy can only be further reduced by droplet diffusion and coagulation. The assumption of a spherical shape is also consistent with mechanical equilibrium. A flat interface will have equal pressure on both sides whereas a curved interface will experience a force (surface tension) acting to minimise the curvature. For this curvature to be stationary there must be a region of relatively higher pressure inside the drop and hence a pressure jump when crossing the interface. This is called the Laplace pressure [3]. It is inversely proportional to the radius and in an isolated drop will act to equalise the curvatures forcing material from high curvature regions to low. For a sphere the pressure difference incurred when crossing the interface is $\Delta p = 2\sigma/r$, where σ is again the surface tension and r is the drop radius. A simple derivation of the Laplace pressure can be done by considering a hemisphere of radius r with pressure Δp inside and pressure p outside. The force exerted on the base of the hemisphere due to the pressure difference must equal that due to the surface tension for a stable shape to exist and so $\Delta p \pi r^2 = \sigma 2\pi r$.

The above thermodynamic results underlie the algorithm 'Ludwig' used here to simulate binary fluids; details of which are given in Chapter 3.4.

Chapter 3

Computational methods

3.1 Introduction

3.1.1 Lattice Boltzmann

The lattice Boltzmann method of simulating fluid systems is a mesoscopic model bridging the gap between microscopic and macroscopic methods.

Molecular models simulate a collection of many particles (the more the better) and their interactions, with the macroscopic behaviour being obtained by looking at large scales in the system. Although computationally intensive this method has the advantage that the macroscopic behaviour arises solely from the microscopic interactions and no assumptions enter the simulation - this advantage is retained in part in the lattice Boltzmann technique. Developments to the microscopic approach took the form of abstractions and simplifications, the most relevant here being the lattice gas automata method where particles are restricted to reside on regular lattice sites and move with identical speeds, and so removing the correspondence with physical particles [4], [11].

Particle populations, $n_i(\mathbf{x}, t)$ take the place of actual particles, where i is a lattice direction in which the 'particle' may move, and reside at each lattice site $\mathbf{x}$. A simple exclusion rule is included, $n_i(\mathbf{x}, t) = 0, 1$ where 0 means no particle and 1 means exactly one particle; hence only one particle can occupy each state and the equilibrium distribution is a Fermi-Dirac distribution.

These 'particles' are propogated from site to site along the lattice directions/vectors, where they collide and mix according to specific rules [5].

As it stands, to get any physical quantities from this type of simulation requires the lattice data to be coarse grained to average out small scale fluctuations; this has the effect of essentially reducing the system size simulated. In order to avoid this a further simplification is implemented and the idea of particles is superseded by that of probability distribution functions f_i. That is, we now work directly with locally averaged quantities so that the (local) particle density at a lattice site is given by

$$\rho(\mathbf{x},t) = \sum_{i=0}^{m} f_i \tag{3.1}$$

where $i = 0$ is the null velocity case and $i = 1..., m$ are lattice directions.

Analogous with particles the distribution functions, f_i, are propagated along lattice directions $\mathbf{c}_i$ now with speeds $|\mathbf{c}_i|$; this also ensures that the f_i's are moved along exactly one lattice site at each time step. Other physical quantities are obtained from the moments of the distribution function. In particular,

$$\rho(\mathbf{x},t)u_\alpha(\mathbf{x},t) = \sum_{i=1}^{m} f_i c_{i\alpha} \tag{3.2}$$

gives the momentum density, and the quantity

$$\Sigma_{\alpha\beta}(\mathbf{x},t) = \sum_{i=1}^{m} f_i c_{i\alpha} c_{i\beta} \tag{3.3}$$

describes the momentum flux. Greek indices denote cartesian coordinates. Higher order moments of the equilibrium distribution function are chosen in order that the desired continuum dynamics of a non-ideal one component fluid are correctly described by the equations governing the system. Note that,

$$\sum_{i=1}^{m} f_i^{eq}(\mathbf{x},t) c_{i\alpha} c_{i\beta} = P_{\alpha\beta} + n u_\alpha u_\beta \tag{3.4}$$

where $P_{\alpha\beta}$ is the pressure tensor, describing the hydrostatic/thermodynamic pressure of a fluid in equilibrium and $nu_\alpha u_\beta$ is the contribution due to the advection of momentum.

The distribution functions, f_i, evolve according to the lattice Boltzmann equation using a simplified collision step (BGK approximation) [2]

$$f_i(\mathbf{x} + \mathbf{c}_i\Delta t, t + \Delta t) = f_i(\mathbf{x}, t) - \frac{1}{\tau}[f_i(\mathbf{x}, t) - f_i^{eq}(\mathbf{x}, t)] \tag{3.5}$$

where $f_i^{eq}(\mathbf{x}, t)$ denotes the equilibrium distribution function.

The RHS of this equation can be viewed of as a collision (or mixing) step; LHS as a streaming (or propogation) step.

It is essential that the correct continuum equations for a fluid system can be reproduced from the lattice Boltzmann equation; that is the continuity and Navier Stokes equation. This can be shown to be the case by Taylor expanding the lattice Boltzmann equation (eq 3.5) up to second order, summing over the velocities and using the conservation of mass, momentum and order parameter and the suitably defined higher order moments of $f_i^{eq}(\mathbf{x}, t)$ (see section 3.3) [22].

The (macroscopic) scales of interest should also be much larger than any set by Δt or $|c_i|$.

3.2 Simulating a Binary Fluid System

For a two component fluid it is necessary to introduce a second distribution function, g_i, corresponding to the order parameter (or fluid composition), to model the system dynamics correctly. Its evolution is governed similary to the f_i's,

$$g_i(\mathbf{x} + \mathbf{c}_i\Delta t, t + \Delta t) - g_i(\mathbf{x}, t) = -\frac{1}{\tau_2}[g_i(\mathbf{x}, t) - g_i^{eq}(\mathbf{x}, t)] \tag{3.6}$$

In these simulations the relaxation parameter $\frac{1}{\tau_2}$ is set to unity ensuring that the order parameter field $\phi(\mathbf{x}, t)$ always relaxes back to local equilibrium after each time step.

As with the single component fluid the physical quantities are given by moments of distribution functions. The order parameter is given at each lattice site by,

$$\phi(\mathbf{x}, t) = \sum_{i=0}^{m} g_i \tag{3.7}$$

and the order parameter flux/advection obeys

$$\phi(\mathrm{x},t)u_\alpha = \sum_{i=1}^{m} g_i^{eq} c_{i\alpha} \tag{3.8}$$

and

$$\sum_{i=1}^{m} g_i^{eq} c_{i\alpha} c_{i\beta} = M\Delta\mu\delta_{\alpha\beta} + \phi u_\alpha u_\beta \tag{3.9}$$

where M is the mobility which controls the rate of diffusion, $\Delta\mu$ is the chemical potential difference between the two components and $\delta_{\alpha\beta}$ is the Dirac delta function. As with the analogous equation for the f_i's the $\phi u_\alpha u_\beta$ term is due to the advection of the order parameter current. Again the above choice is made so that the correct hydrodynamics result [22]. Mass conservation is imposed and following the same procedure of Taylor expanding equation(3.6), substitutions and approximations (as with the f_i's) a convection-diffusion equation can be derived which governs the evolution of the order parameter. The resulting equations are given in section 3.3 below.

The lattice Boltzmann method can be viewed as a collision or mixing step and a streaming or propogation step. At the mixing step the distribution functions relax towards equilibrium and the relaxation time, τ for the density distribution functions f_i is controlled by the viscosity parameter (diffusion of momentum) η via $\eta = (\frac{2}{\tau_1} - 1)/6$. For a binary fluid the distribution functions, g_i have associated with them a relaxation time, τ_2. In our work τ_2 is set to unity ensuring the order parameter field relaxes back to equilibrium at each time step (this is more economic computationally).

3.2.1 Lattice isotropy

For the simulation to reproduce the required hydrodynamics when governed by the equations in the above section, several things must be considered carefully.

Macroscopically the hydrodynamic properties of the fluid must be isotropic and bear no evidence of the underlying lattice. Suitably symmetric lattices are for example, triangular and hexagonal lattices.

Our two dimensional simulations are done using a nine velocity lattice with four nearest neighbours of velocity $= 1$ and four next nearest neighbours with velocity $= \sqrt{2}$ and include a zero velocity vector. See 3.4.1 for more lattice details.

Conservation of mass, order parameter and momentum must be adhered to locally and at each time step. This is satified by implementing the following constraints,

$$\sum_{i=0}^{m} f_i^{eq} - f_i = 0 \tag{3.10}$$

$$\sum_{i=0}^{m} f_i^{eq}\mathbf{c}_i - f_i\mathbf{c}_i = 0 \tag{3.11}$$

$$\sum_{i=0}^{m} g_i^{eq} - g_i = 0 \tag{3.12}$$

where the sum is over the $i = 1, ...m$ lattice directions at each site and the null velocity case.

It is also necessary to specify the equilibrium distributions in order to simulate the required fluid characteristics. This is done by assuming a velocity expansion form for them up to second order,

$$f_i^{eq} = \rho\omega_\nu \left\{ A_\nu + 3u_\alpha c_{i\alpha} + \frac{9}{2}u_\alpha c_{i\alpha}u_\beta c_{i\beta} - \frac{3}{2}u^2 + G_{\alpha\beta}c_{i\beta}c_{i\alpha} \right\} \tag{3.13}$$

where ω_ν, A_ν and $G_{\alpha\beta}$ are constants the value of which are found by using the conservation restrictions, the second order moment of the equilibrium distribution function and the symmetry considerations of the lattice. The index ν denotes the speed: 0, 1, or $\sqrt{3}$. An analogous procedure is performed for g_i^{eq} which produces an identical equation to the above with different choices for coefficients A_ν and $G_{\alpha\beta}$.

3.3 Equations of motion

Governing the dynamics of the system are a convection/diffusion equation which describes the evolution of the order parameter

$$\partial\phi/\partial t + \mathbf{u}.\nabla\phi = M\nabla^2\mu \tag{3.14}$$

and the Navier Stokes equation, which describes the motion of the fluid,

$$\rho\left[\partial\mathbf{u}/\partial t + \mathbf{u}.\nabla\mathbf{u}\right] = \eta\nabla^2\mathbf{u} - \nabla.\underline{\underline{P}} \tag{3.15}$$

where $\underline{\underline{P}}$ is the stress tensor. For this system, it may be shown that $\nabla.\underline{\underline{P}} = \nabla p - \phi\nabla\mu$, where p is a scalar pressure and $\phi\nabla\mu$ can be viewed as a body force caused by the interactions between the two fluids [10].

In the continuum limit the equations of motion for an incompressible fluid, given above, can be derived from the lattice Boltzmann equations for the g_i and f_i distribution functions respectively, as well as a continuity equation. This is done by expressing them as a Taylor expansion up to second order and writing f_i (g_i) in terms of f_i^{eq} (g_i^{eq}) and its derivatives respectively. Summing the resulting equations over the velocities and using conservation of mass, order parameter and momentum and the expressions for the higher order moments of the distribution function, along with appropriate approximations gives the correct continuum equations. Additional terms arise from this derivation however they are small in practise [22].

3.4 Ludwig

Ludwig was written by J.-C. Desplat, I. Pagonabarraga and P. Bladon. For full details see [5].

3.4.1 Algorithm

A 'ϕ^4' model is chosen to model the free energy of the phase separating system, as in eq 2.3

$$F[\phi] = \int \{\frac{A}{2}\phi^2 + \frac{B}{4}\phi^4 + \frac{\kappa}{2}(\nabla\phi)^2 + \frac{1}{3}\rho ln\rho\}dx \tag{3.16}$$

In order to achieve the double well form necessary for phase separation, the constant A is negative. By setting $\delta F[\phi]/\delta\phi = 0$, the equilibrium order parameter ϕ^* is found: $\phi^* = \pm\sqrt{-A/B}$. For simplicity we choose parameters to ensure $\phi^* = \pm 1$ and so $A = -B$. The total fluid density ρ is set to unity in equilibrium. In using Ludwig for binary flows one should check that ρ does not vary by more than a few percent.

These parameters, A and B along with κ determine the interfacial tension from eq 2.10, as $\sigma = \sqrt{(-8\kappa A^3/9B^2)}$ and the interfacial width is given by $\xi_o = \sqrt{-\kappa/2A}$ [3] see section 2.2.

Another important parameter in the simulation that doesn't enter the thermodynamics is the mobility, M, which controls the 'strength' of the diffusion. Considerations in setting its optimal value are given in section 5.1.1 and 5.1.3.

For three dimensional simulations, Ludwig is set up to use a body centred cubic lattice (see fig 3.1) which has 15 velocity vectors. Six vectors correspond to the nearest neighbours of a given lattice point and have velocity $= 1$; eight vectors correspond to the next, next nearest neighbours and have velocity $\sqrt{3}$. There is also a vector with zero velocity corresponding to the rest particle at that node. The velocity associated with each vector is equal to its magnitude.

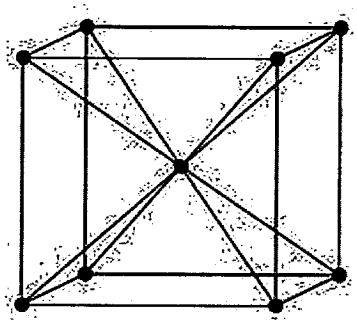

Figure 3.1: body centred cubic lattice showing the eight diagonal next, next nearest velocity vectors only

For the two dimensional simulations done here a simple square lattice is used with nearest and next nearest neighbour interactions. This is effectively a slice taken through the three dimensional lattice and is the equivalent of a nine component velocity model including a zero velocity distribution function residing at the lattice node. With the periodic boundary conditions in place the lattice vectors propagating out of the plane are 'wrapped' round and constitute the incoming vectors on the other side. This has allowed use of the Ludwig code [5] for two dimensional work taking advantage of extensive development work done on the code.

Chapter 4

2D Drop Breakup

4.1 System of interest

For the main runs a lattice size of 120×400 lattice units is used. Simulations are also done on a smaller lattice of 60×100 for comparison. In the shear direction the system has periodic boundary conditions and for the more viscous systems it is a possibility that a deformed drop may be influenced by its periodic neighbour. Perpendicular to this there are solid walls which have 'non-slip' boundary conditions. Giving opposite walls equal and opposite velocites the layer of fluid next to them will be dragged along at the same velocity. Due to the fluid viscosity momentum will diffuse through the system on a time scale set by the kinematic viscosity ($[\nu] = [L][T]^{-2}$) and generate a simple shear profile,

$$\mathbf{u} = \dot{\gamma} \begin{pmatrix} 0 \\ x \end{pmatrix} \tag{4.1}$$

where $\dot{\gamma}$ is the shear rate and (x, y) a cartesian coordinate set.

At the centre of the lattice a droplet is initialised with a radius of 21 lattice units (or 10.5 in the smaller system) and order parameter $\phi = -0.97$. The surrounding fluid is set with an order parameter of $\phi = +0.97$. Initialising the system with order parameters slightly off their equilibrium values was an attempt to inhibit the drop evaporating (see chapter 5.1.2) by causing diffusion of material into the drop and so re-establish equilibrium concentration. A diagram of the system is given below in fig (4.1).

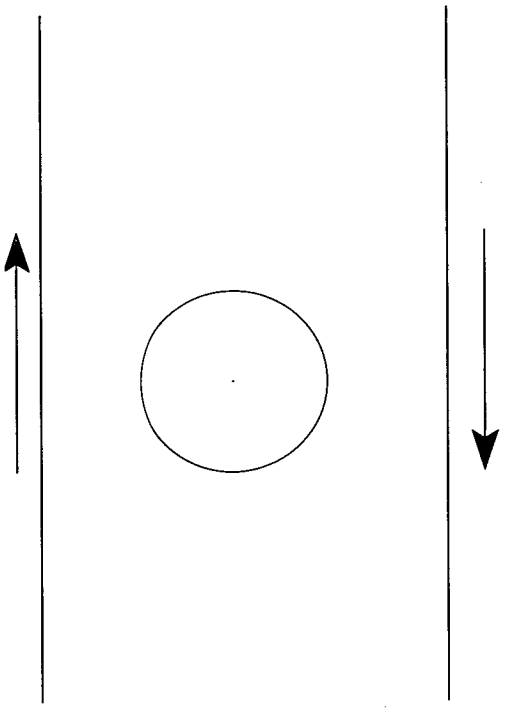

Figure 4.1: schematic diagram of system

As the system is sheared the viscous stresses will pull and deform the drop, rotating it towards the flow lines, whilst surface tension will act to oppose this deformation. Surface tension acts to minimise the surface area and hence free energy. Another way of understanding this is with the Laplace pressure. This will act to minimise and equalise the curvatures. The aim of the simulations is to find, as a function of shear rate $\dot{\gamma}$, the point where the shear stress just balances the restoring force due to surface tension, and then find the value of $\dot{\gamma}$ beyond which no stable drop shape exists and the drop breaks.

The study of such problems is not straightforward since they involve the interaction and coupling of thermodynamics and hydrodynamics; the shear stresses pull and deform the drop whilst surface tension acts to oppose this and in turn generates fluid motion which is superimposed on the shear flow, so the droplet shape influences the fluid motion which in turn influences the droplet shape. This can be seen in the Navier Stokes equation for the system, in which the gradient of the pressure tensor has a term $-\phi\nabla\mu$ in it which couples the fluid flow to the evolution of the order parameter. The parameter space of this problem is also not small.

4.2 Previous studies

Drop deformation and breakup has long been an area of interest both theoretically, experimentally and numerically. For example Savart (1833) [18] investigated the decay of a jet of water due to the growth of perturbations on its surface. Plateau (1849) [12] showed that surface tension was the cause of the breakup.

By considering sinusoidal perturbations on a fluid cylinder of radius r, Rayleigh (1879) [15] discovered that these grew most rapidly if they had a wavelength of $\lambda \sim 9r$. Conditions for deformation and burst of drops were studied experimentally and theoretically by Taylor (1932/34) [23], [24]. Various viscosity ratios of drop to fluid matrix were looked at, for pure extensional flow (using a 'four roll' method) and simple shear (using a 'parallel band'). For the case of equal viscosities he found that the capillary number necessary to induce burst in simple shear was 0.5 (and 0.4 in pure extensional flow).

An experimental study is done by Bentley and Leal (1985) [1] which looks at the equilibrium deformation and orientation of drops in steady flows as a function of the capillary number for various flow types and viscosity ratios as well as the critical capillary number required for drop burst as a function of flow type and viscosity ratio. Again these experiments are carried out at low Reynolds numbers. In order to study conditions for drop breakup a computer controlled four roll mill method is used to generate flows ranging from pure extensional to flows with increasing vorticity, however this terminates before simple shear is reached. It is pointed out that not only the instantaneous flow conditions contribute to drop break but the whole time history of the velocity gradient. The flow strength here is increased slowly so that the drop progresses through a series of equilibrium states. Results are compared with asymptotic deformation theories and with numerical studies.

Theoretically and numerically the difficulty in this problem of drop deformation and breakup is that the governing equations of motion (Navier Stokes, continuity) have to be solved both inside and outside the drop and boundary conditions implemented at the interface. However the shape of the interface is not known beforehand, but arises as part of the solution.

Much theory has been done on drops in 3 dimensions, for example deformation and burst conditions of drops with various viscosity ratios to the surrounding fluid matrix, and for various types of fluid flow i.e. from simple shear to parabolic. The majority of these theories are done

at zero Reynolds number due to the simplifications this yields. Rallison (1980) [13] undertakes a numerical study of time dependent deformation and conditions for drop burst in shear flows ranging from pure rotational through simple shear to pure extensional/hyperbolic flow. This is carried out at zero Reynolds number and the drop and fluid matrix have equal viscosities. The capillary number (shear rate) is increased "very gradually" to its final value and it is noted that the critical capillary number may be dependent on the way in which the capillary number/shear rate is increased. Results are compared with experiments and with asymptotic deformation theories.

In 3 dimensions, the precise point of breakup where an extended drop develops a slender neck which then pinches off into two separate parts presents a theoretical challenge. Here, due to the infinite (second) curvature necessary at this point, the governing equations of motion become singular. This singularity is confined to a very small area so that outwith this the time scale is static in comparison. Microscopic interactions are only relevant within this small region and thus, outwith this, solutions for the Navier Stokes equations may be found before and after the pinch off and continued through the singularity (Eggers 1995) [6].

Using a lattice BGK fluid Halliday et al (1996) [8] simulate the burst of neutrally buoyant drops in 2 dimensions in fluid matrix of equal viscosity in shear flow. Each fluid component is associated with a colour and phase separation is effected by maximising the colour gradient. The critical shear rate is ascertained by 'increasing the applied shear rate' and is done for a range of radii ($10 < R < 20$) and surface tensions. Lattice dimensions were varied to minimize size effects. The drop orientation is also noted. Results were compared from drops with different initial radii when overall lattice proportions were scaled with the initial radius. Xi and Duncan (1999) [27] also use a lattice Boltzmann algorithm to simulate the deformation and breakup of 3 dimensional drops in simple shear. Small and large deformations are obtained by initialising the shear rate at the 'final' value.

A numerical investigation of the influence of inertia on drop breakup in 3 dimensions in simple shear is undertaken by Renardy and Cristini (2000) [16]. Most interesting here is the suggestion of some kind of Bernoulli effect/aerodynamic lift mechanism which 'pulls' the higher viscosity drops towards the walls where they experience a greater shear rate. This is contrasted to behaviour in Stokes flow which rotates the drop towards the flow lines where a minimum of shear is experienced. A later paper by the same authors [17] discusses the effect of inertia on the size of the daughter drops.

Two dimensional drops in simple shear are investigated by Wagner and Yeomans (1997) [26]. They used lattice Boltzmann simulations to study the effects of shear flow on an equilibrium 2 dimensional drop in a phase separated binary mixture. The thermodynamics of drop dissolution in equilibrium is discussed with respect to the drop volume relative to the total system size. Tip streaming in drops under shear is also mentioned as a mechanism by which drops may dissolve, and how this can be, to some degree, compensated for by careful selection of the parameters.

A similar study is by Sheth and Pozrikidis (1994) [19]. They look at the role of inertia in drop breakup in 2 dimensions using a similar system to that used in the study here; that is, drops are situated midway between two solid walls which generate shear flow and have periodic neighbours. The dimensions are given as $L/2H = 1$ and $r/H = 0.5$ where r is the drop radius, L corresponds to the length of the simulation box in the x direction and H to that in the y direction in our simulations. This lattice is considerably smaller than used here, however, there are no checks made as to the influence of the solid walls or periodic neighbouring drop. Drops are suddenly introduced into the shear flow and allowed either to evolve into a stable shape or continue deforming and breakup. The system parameters are the Reynolds number, capillary number (or in the case of more inertial flows the Weber number which expresses the relative magnitude of inertial to capillary forces) and the viscosity ratio of the drop to the surrounding fluid ($\lambda = 1, 10$). By fixing the capillary number for a given viscosity ratio they vary the Reynolds number: $Re = 1, 10, 50, 100$, and look at the deformation produced. The different shapes are shown as well as streamlines and vectors of the velocity fields. Plots of deformation against time are given. It is noted that inertial effects may promote deformation and breakup opposed to the stabilising effect of viscosity and surface tension. In order to study this more fully the distribution of shear stress along the upper wall is plotted as well as the drag force exerted on the upper (or lower) wall. The structure of the vorticity field is also examined.

Lattice Boltzmann simulation techniques are much suited to this type of problem due to the fact that the singularity in the fluid equations of motion at the point of break up is avoided. Instead of modelling the interface as an internal, singular boundary it is represented as a smooth function of $\phi(\mathbf{x}, t)$.

4.3 Velocity Ramp

The work undertaken here is the first thorough study (that we know of) of the effect of finite Reynolds number on droplet breakup in two dimensions.

The aim of these simulations is to determine the critical capillary number for breakup of a droplet in the system described in the above section and to ascertain what influence inertia plays in the process.

To pin point the critical capillary number for each parameter set it was decided to take the drop through a series of, as near as possible, equilibrium states. It is anticipated that this method will give the maximum capillary number necessary to cause drop break in such a system. The flow history is known to be important in influencing break and in particular a 'sudden startup' method, whereby the shear rate is initialised at the critical number, will initiate breakup below the critical capillary number as defined here.

Tests on a smaller lattice were initially undertaken using a 'continuous' ramp where the ramp was increased at every time step. This meant establishing the highest possible increment of shear below which all results converged. (See section (6.5.1)). If the increase in shear is too large there will be insufficient time for this shear step to propogate through the system, induce a deformation in the drop and for it to relax back to an equilibrium state before the next time step, i.e. the deformation will 'lag' behind the capillary number. This can be avoided with a slow enough ramp. However this method would prove very time consuming on a larger lattice. In an attempt to make the ramping process more efficient an algorithm was devised to take the drop up to as near the critical capillary number as possible.

4.3.1 Unrestricted ramp

Starting with the system as described above an initial shear increment is defined, $\Delta\dot{\gamma}$. Measuring the deformation of the droplet (defined in equation 5.6) every 50 timesteps or so, the present value is compared with the previous, and the time taken Δt for the difference in these values to fall below 10^{-4} noted. The simulation is then run on for $3\Delta t$ to ensure the drop has deformed and relaxed back to an equilibrium shape. Before incrementing the ramp again the drop is recentred (as, in some preliminary simulations, it would move slightly off centre causing it to

gain a small amount of momentum and traverse round the lattice). Before increasing the shear profile the current configuration is saved. If the result of the shear increase is to cause the drop to break the previous configuration is restored and the shear increment reduced by half, $\Delta\dot{\gamma}/2$ and the process repeated until the increment in shear rate is below a set threshold and the desired accuracy has been achieved.

Completion of the simulation is accomplished when the ramp has refined itself to a given accuracy; in most cases this is that the increment of the ramp is halfed until less than 10^{-4} times the original rampstep velocity.

4.3.2 Restricted ramp

As well as performing the above with no restriction on the deformation in response to an increase in shear the same input sets were rerun with the deformation difference being constraint to less than 0.05. If this was exceeded, again the previous configuration was reloaded and the shear increment halfed.

The restricted (unrestricted) methods of ramping can also be thought of as 'fast' ('slow') ramps respectively; the latter taking the drop arbitrarily slowly up to the point of breakup whilst the former method allows the process to take place quickly with the drop deforming freely to each increase in rampstep.

Plots of deformation with time for viscosities $\nu = 0.2362$ and $\nu = 0.8768$ are given in fig 4.1 and show the reaction of the drop to an increase in shear. The former is one of the least viscous runs and clearly shows an 'overshoot' in the deformation in reponse to the increase in shear then a flattening off as shear stress and surface tension reach a balance point; almost reminiscent of a damped harmonic oscillator. This overshoot is not present in more viscous drops.

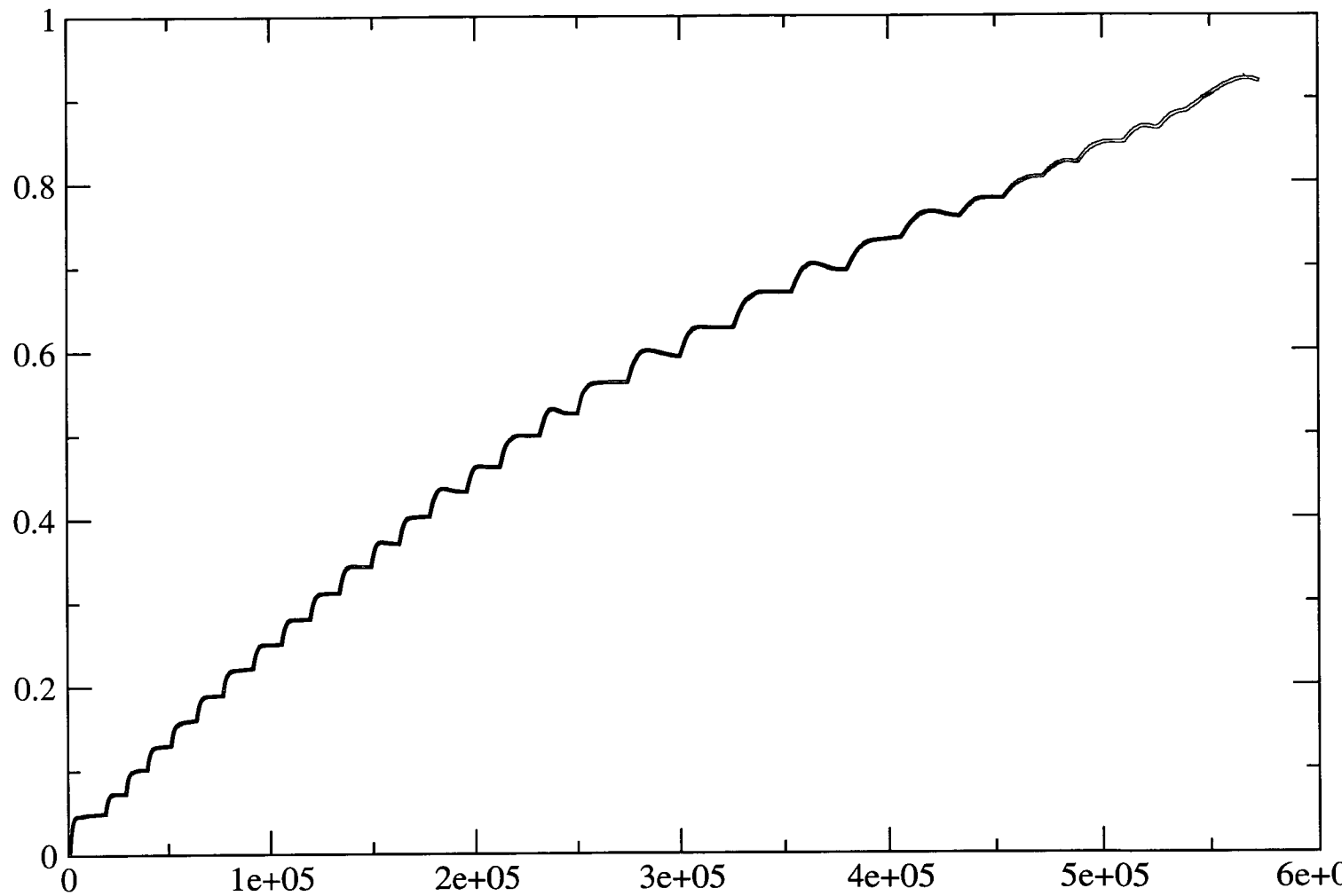

Figure 4.2: Deformation with time for drop viscosity $\nu = 0.8768$. The lattice size is 120x400, and the radius is initialised as $R_0 = 21$; initial shear increment = 1.67 x 10^{-4} and final shear rate = 2.66 x10^{-3}.
Note that R is not constant over the course of the simulation, see 5.2.4.

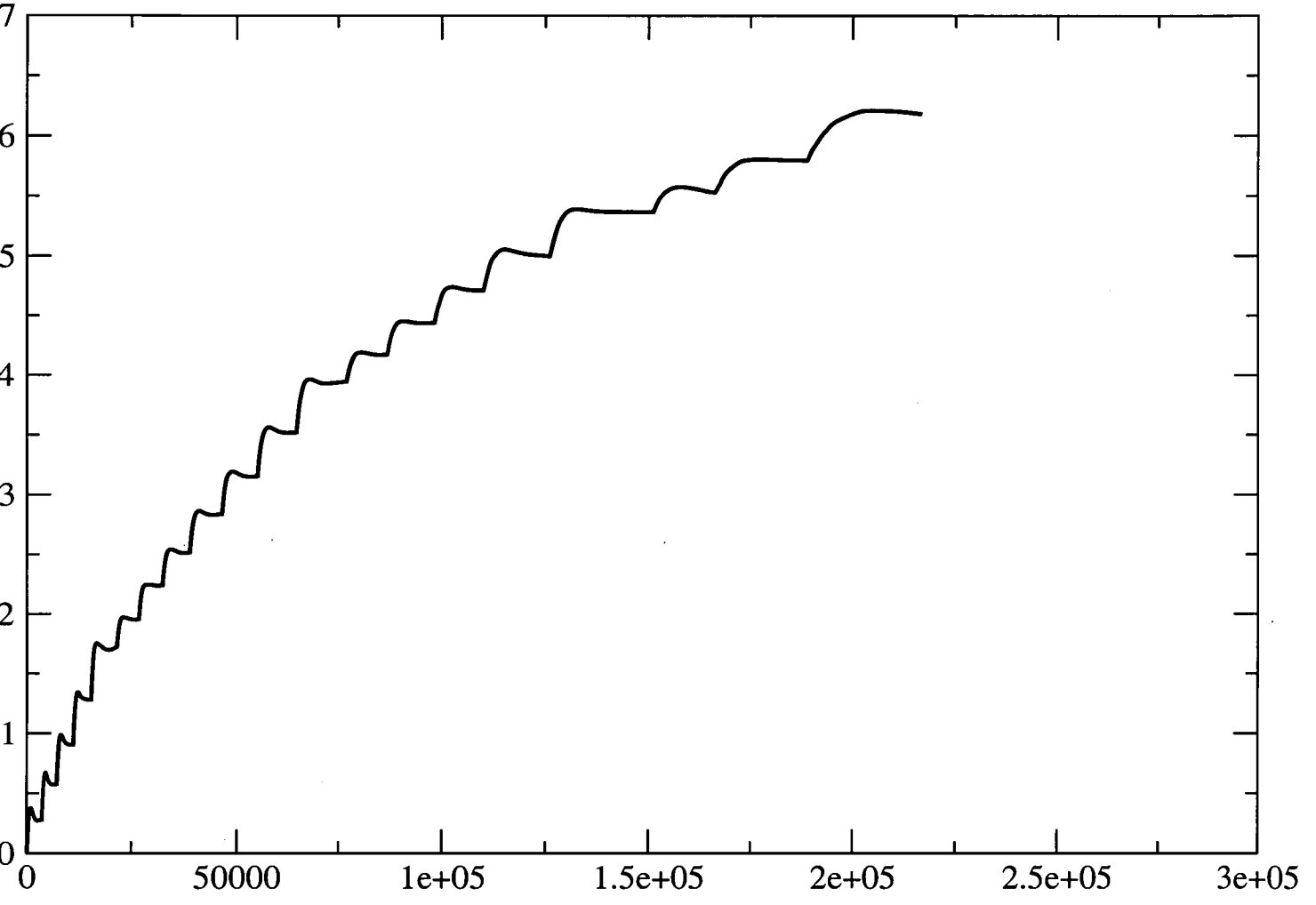

Figure 4.3: Deformation with time for drop viscosity $\nu = 0.2362$. The final shear rate is 1.68 x 10^{-3}. Other parameters are as given in fig 4.2.

Chapter 5

Analysis and Validation

5.1 Analysis method

To characterise the state of the system several dimensionless parameters are introduced. Firstly the capillary number which expresses the balance of shearing stress and surface tension,

$$Ca = \frac{\eta \dot{\gamma} R_0}{\sigma} \tag{5.1}$$

where η is the viscosity, $\dot{\gamma}$ the shear rate, σ is the surface tension and R_0 is the radius of the undeformed drop. The Reynolds number gives the relative importance of inertial versus viscous forces,

$$Re = \frac{\rho \dot{\gamma} R_0^2}{\eta} \tag{5.2}$$

To gauge how deformed the drop is the following moments are calculated,

$$b = \sum_i \theta(\phi)\phi \tag{5.3}$$

$$c_\alpha = \sum_i \theta(\phi) x_\alpha \tag{5.4}$$

$$d_{\alpha\beta} = \sum_i \theta(\phi)\phi(x_\alpha - c_\alpha)(x_\beta - c_\beta) \tag{5.5}$$

where θ is the Heaviside function. The sums are over all lattice sites where x_α is the lattice cartesian coordinate of that site with respect to a chosen origin. Hence b is equivalent to the drop volume and is calculated by summing the order parameter at each lattice site within the drop. It is from this that the length scale R_0 is calculated i.e. $R_0 = \sqrt{(b/\pi)}$. Doing so compensates for any dissolution (unless dissolution is very strong then it is apparent from the results; see later). The ratio c_α/b gives the lattice cartesian coordinates of the centre of mass of the drop and the eigenvalues of $d_{\alpha\beta}/b$ gives two length scales, $\sqrt{X}$ and $\sqrt{Y}$, the semi major and minor axis of an ellipse. Using these the deformation of the drop is defined,

$$D = \frac{\sqrt{X} - \sqrt{Y}}{\sqrt{X} + \sqrt{Y}} \tag{5.6}$$

For the highly deformed structures as produced in the higher viscosity runs the above estimation of the deformation may not be that representative since it assumes an elliptical shape; note that $D \to 1$ is the limit of a long thin drop in any case.

The 'velocity ramp' algorithm as detailed in section 4.3 is used to take the drop through a series of equilibrium states until a stable shape is no longer sustainable and the drop breaks.

Measurements of the deformation (and drop volume) are taken every 50 time steps and the capillary and Reynolds number are calculated when the drop reaches a steady state; before the next shear increment.

5.2 Simulation parameters and limitations

5.2.1 Simulation parameters

All parameters are measured in lattice units which are derived by taking one lattice spacing as a unit of length, one time step as the time unit and mass from the density which has here been set to unity. The value of the surface tension used for all the simulations is $\sigma = 0.0456$ and the mobility was chosen to be $M = 3.0$. The criteria for choosing M are discussed in 5.1. Constants A, B and κ in equation 3.16 take the values $-A, B = 0.06$, $\kappa = 0.03899$. These determine the interfacial width and the surface tension (see section 3.4.1). A range of viscosities were used ranging from $0.181 - 0.8768$, with an approximately equal ratio between successive shear rates of ~ 1.3. These are listed in table 5.1 below.

run	ν
0	0.181
1	0.2362
2a	0.271
2	0.307
2b	0.335
2c	0.367
3	0.399
4	0.519
5	0.6746
6	0.8768

Table 5.1: table of viscosities used in simulations

For the main results in this study a lattice size 120×400 and a drop radius of 21 lattice units are used. Note that the viscosity given for run 0 did not run to completion due to simulation instabilities (see section 5.3).

5.2.2 Consequences of underlying lattice anisotropy

Lattice artifacts present in the simulation can limit the accuracy of the results if neglected. Parameters cannot be set arbitrarily and consideration is needed to reach a balance between physical accuracy and computational efficiency.

Looking at a single stationary droplet of one fluid in another which has been allowed to reach equilibrium, it appears to be slightly aspherical (or non circular) in that the interface flattens in the cartesian lattice directions and expands in the lattice diagonals. See [10] and [9] for a detailed discussion. This dependence of interface tension on direction can be removed by increasing the interface width. An interfacial width $\xi = \sqrt{(-\kappa/2A)}$ greater than or equal to the lattice spacing will remove any anisotropy in the interface, however implementation of this is not altogether practicable. For the interface to maintain local equilibrium the order parameter must be able to diffuse over several ξ on time scales much faster than those of the fluid motion, necessitating a large value for the mobility. This may not be desirable as most studies concentrate on the hydrodynamic growth mechanisms and scaling of phase separation in a binary

fluid and a high mobility/diffusion will contaminate a purely hydrodynamic regime. Likewise for droplets we don't want diffusion to strongly interfere with the breakup itself; its role is to maintain the equilibrium interfacial tension. Selecting the value of the mobility is somewhat hit and miss; too large and, particularly in the droplet problem, the simulation becomes unstable and the drop evaporates immediately; too low and the fluid will not be able to maintain local equilibrium across the interface. Curiously enough, in the droplet problem a low value for the mobility also causes significant dissolution which affects the drop shape and interferes with the progression to breakup (see section 5.2.5).

5.2.3 Spurious currents

Spurious currents and diffusive flux of the order parameter are clearly visible in the velocity maps of equilibriated isolated drops and form a 'petaled' pattern about the drop shown in figures 5.1 and 5.2. In both these examples the drop has been allowed to equilibriate for the order of 10^3 time steps. Their origin stems from the forcing terms in the Navier Stokes equation (equation 3.15). The gradient of the pressure tensor is $\nabla.\underline{\underline{P}} = \nabla p - \phi\nabla\mu$. When in equilibrium this must vanish, however due to the discretisation of the equation the terms here do not cancel, leading to a residual forcing term and generating the spurious currents and diffusive fluxes .

It was initially thought that the diffusive flux of the order parameter could be suppressed by decreasing the mobility, however in the study being undertaken this may not be expedient due to reasons given in section 5.2.5.

After allowing a drop to equilibriate, the magnitude of the spurious velocities are of the order 10^{-3} in lattice units which is two orders of magnitude smaller than the wall velocity at the critical breakup point. Diffusive flux of the order parameter in a deformed drop are shown in fig 5.3. These are also of the order 10^{-3}. It is uncertain as to the relative contribution to these fluxes from 'tip streaming' and Laplace pressure considerations (see below), compared to the spurious terms.

5.2.4 Droplet dissolution

In the 2 dimension droplet case, problems are also encountered concerning drop dissolution resulting from free energy balance. In order for a drop to be stable it must be energetically

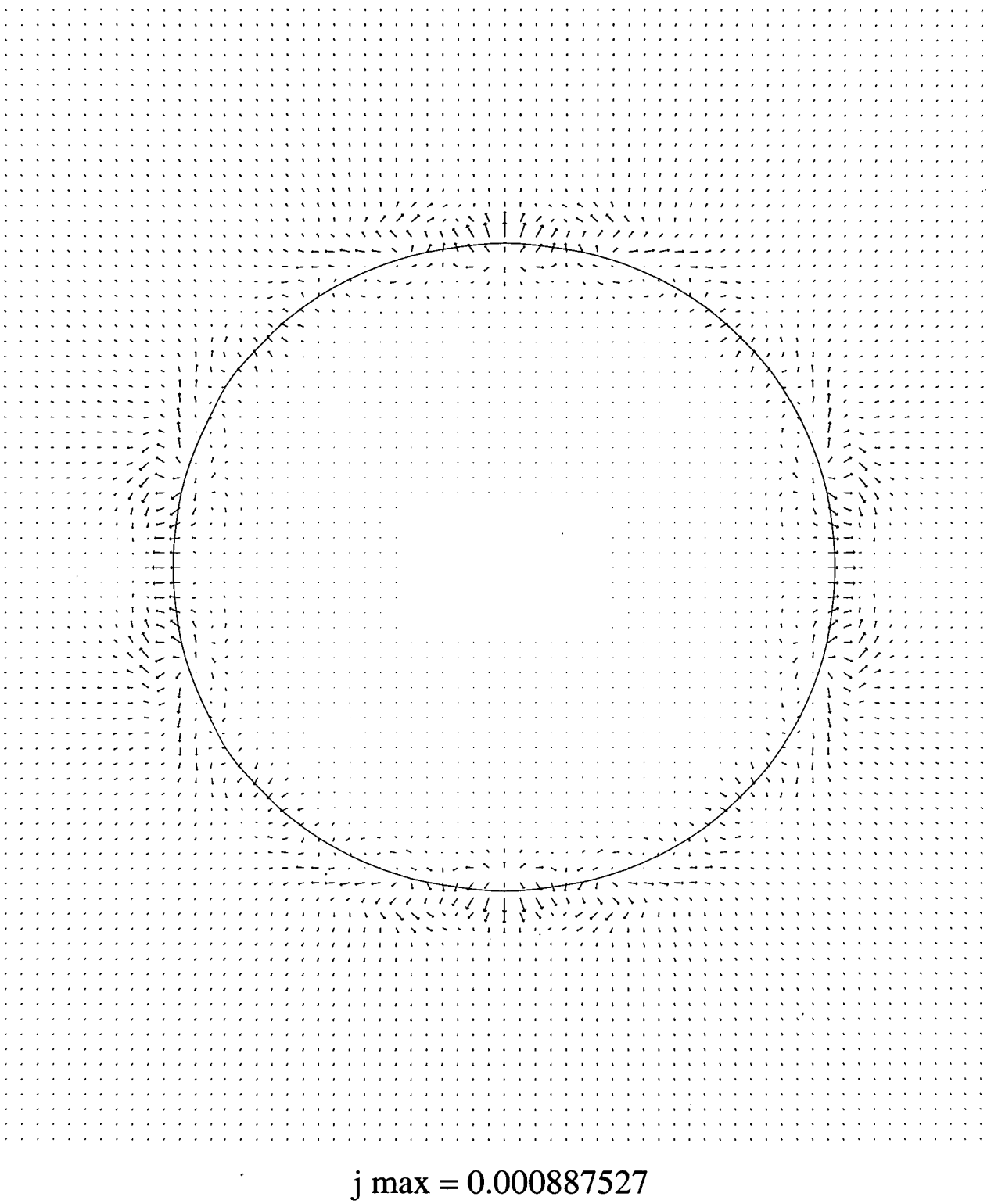

Figure 5.1: Section of lattice 75 x 75 showing the diffusive flux of order parameter in equilibrium. Total lattice size 120 x 400. The arrows give the direction and magnitude of the velocity field; the longest arrow corresponding to $j = j_{max}$. Drop radius $R_0 = 21$, mobility, $M = 3.0$ and viscosity $\nu = 0.519$. Note diffusive flux is seem to increase and viscosity in decreased.

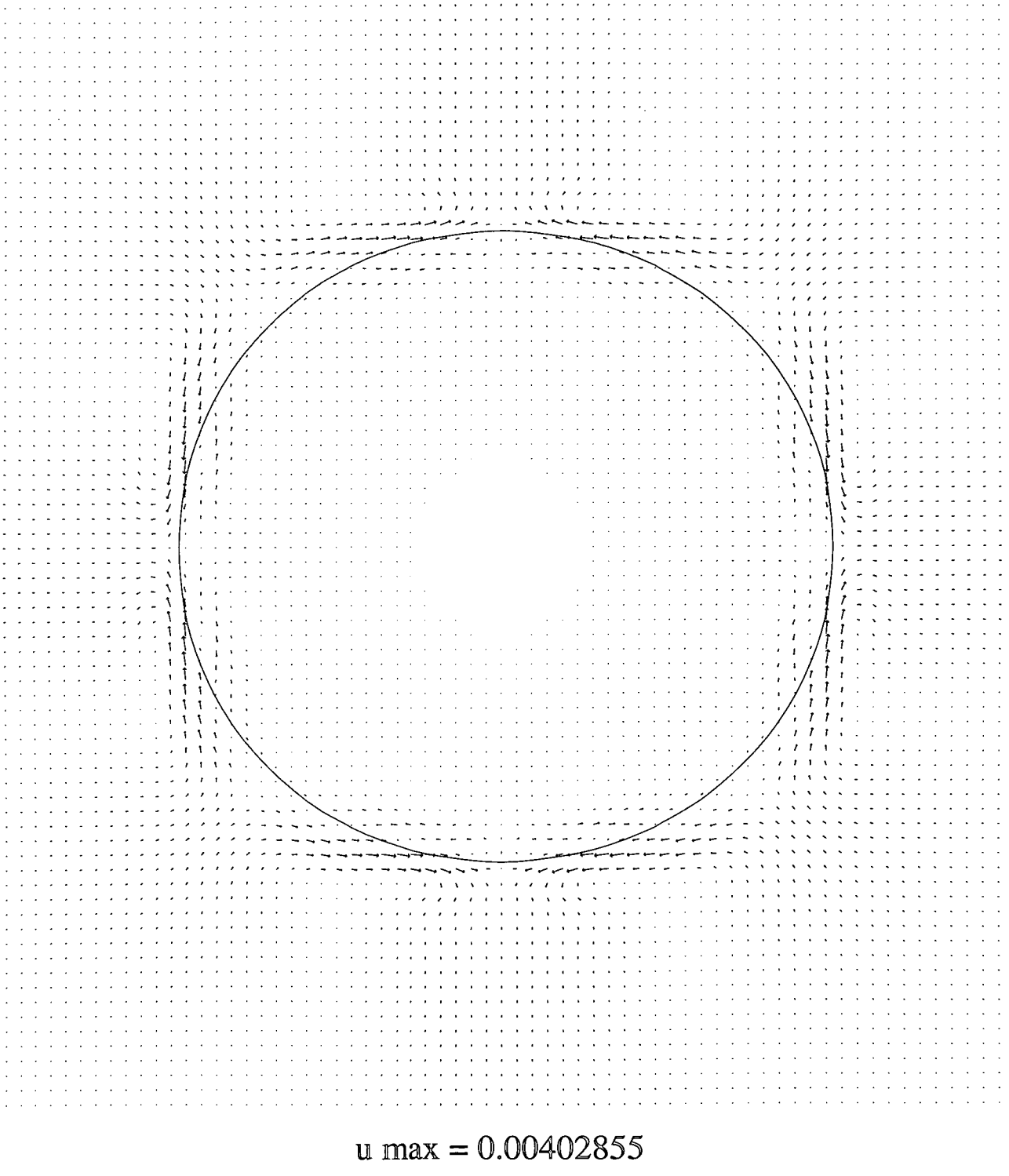

Figure 5.2: Spurious currents in equilibrium. The arrows give the direction and magnitude of the field displayed; the longest arrow corresponding to $u = u_{max}$. System parameters are given in fig 5.1.

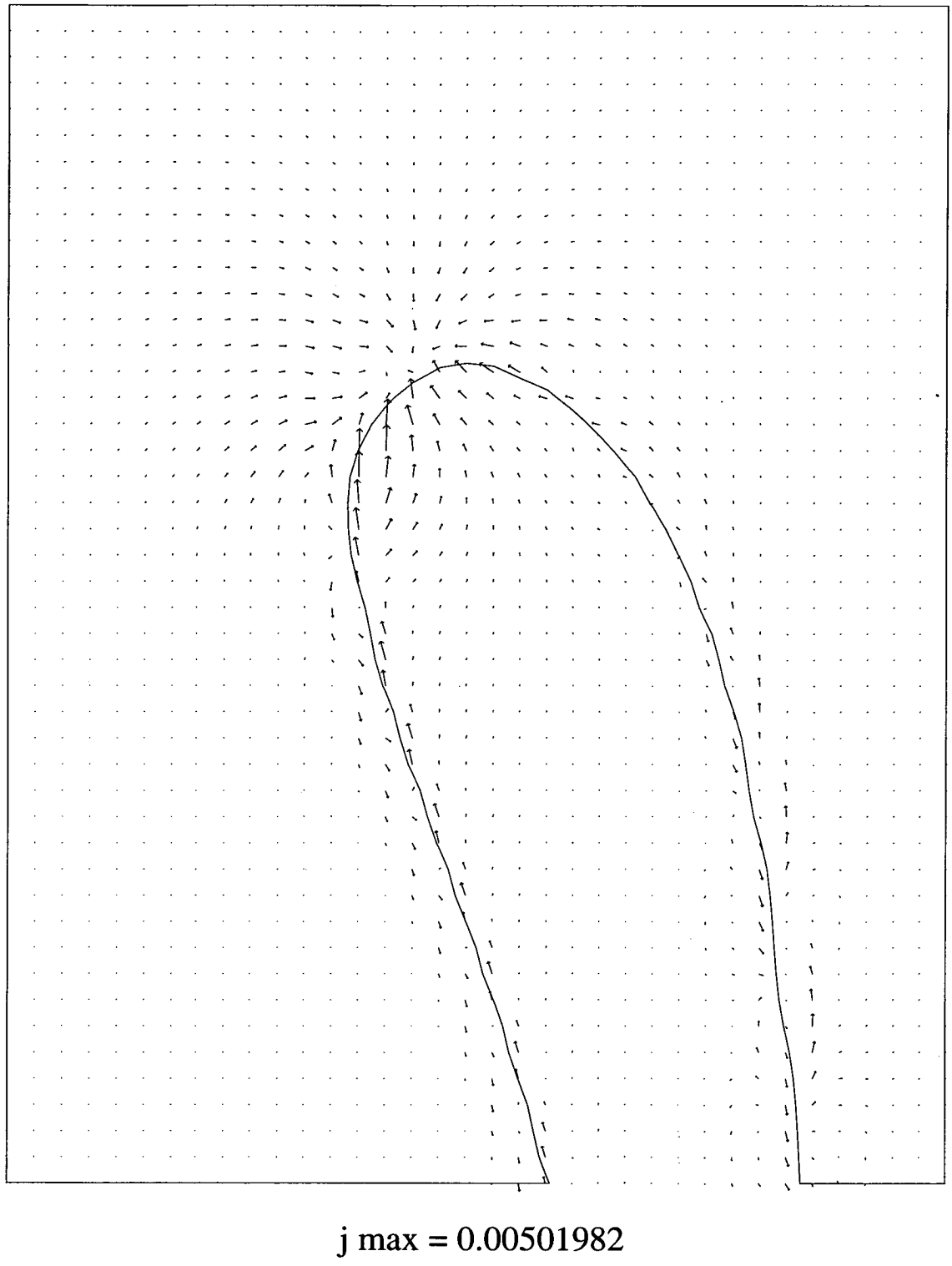

Figure 5.3: diffusive flux in deformed drop taken from figure 6.1h. Frame size 36 x 46. Parameters are given in fig 5.1.

favourable to form two phases separated by an interface, however if the drop is too small the surface energy becomes large relative to the bulk and the drop dissolves to minimise free energy. This is analogous to the process of nucleation or evaporation of water droplets. If there is sufficient water concentration in the ambient air (vapour pressure) the drop will continue to grow; however if this is not the case, the droplet will evaporate due to the large Laplace pressure in an attempt to equilibriate the vapour pressure inside and out. Concentration currents outwith the drop will lead to material being diffused from the drop to bring the phases back to the equilibrium composition; the larger the system the more material will be needed to achieve this. Dissolution will occur if the volume of the drop is small with respect to the total system size. Endeavours to compensate for this non-constant drop volume included setting the order parameter to a slightly off equilibrium value: $-0.97/+0.97$ in the drop and surrounding fluid respectively. This caused material to diffuse into the drop, but was not found to be effective and served only to increase the volume of the drop initially until the equilibrium concentrations were reestablished. In most of the simulations done, when extracting a length scale from the drop it was enough to obtain it from the actual droplet volume at each sample point. This allows compensation for the gradual change in drop volume when calculating the deformation D (eq 5.6) and flow parameters Re and Ca (sections 5.1 & 5.2). However when dissolution was too strong it became particularly apparent, for example in the plot of Re vs Ca as a very marked downward curving that usually precedes the termination of the simulation as the drop's volume becomes too small to be energetically favourable and the drop dissolves.

5.2.5 Tip streaming

For the sheared droplet problem at hand (in two dimensions) another mechanism for dissolution may act. This phenomenon of 'tip streaming' [26] occurs whereby material is physically eroded from the drop by the shear flow and it gradually dissolves. In this case it may be advantageous to increase the mobility. Material dragged from the drop will cause the chemical potential in the drop to decrease and the gradient therefore to be directed towards the drop; increasing the mobility to a maximum (within the bounds of simulation stability) will facilitate the diffusion of material back into the drop. For a small mobility parameter this would necessitate the chemical potential gradient to be large and hence lots of material to be eroded from the drop leading it to dissolve, however for infinite diffusion the material pulled from the drop will be immediately

returned. A related phenomenon has been seen [21] in low viscosity drops in a higher viscosity matrix and has been attributed to the accumulation of surfactant at the tips (although there is no surfactant in our simulations). It is likely that this mechanical erosion of the drop is compounded by the large Laplace pressure at the tips due to the high curvature there, increasing diffusion of material away from the drop in an attempt to equalise curvature and minimise free energy. Diffusion here could be seen to play an analogous role to the surfactant in the experiments.

It had previously been thought that as low a mobility as possible was desirable due to the inhibition of dissolution, as long as it was large enough to keep the interfaces in equilibrium. However for this particular problem it is found that setting the mobility to as high as achievable is now more advantageous. Any dissolution will set up a chemical potential gradient directed towards the drop. With a high mobility this means material can be returned quickly to the drop. However in these simulations it cannot be set arbitrarily large. Even for the highest viscosity simulated here a mobility of $M = 4.0$ caused the simulation to become unstable very quickly. As the choice is somewhat trial and error, a mobility of $M = 3.0$ was found to be the highest integer value giving stable simulations for the whole viscosity range.

To highlight the tip streaming phenomenon and the role of the mobility, the drop radius (calculated from the current drop volume) is plotted against time for mobilities 3.0, 2.0 and 0.3 (see fig 5.4). The initial increase of all plots is due to the offset of the order parameter as previously discussed (section 5.2.4). However the plot with $M = 0.3$ (black plot) increases very little compared to the other two and also begins quickly to dissolve. At this point it was necessary to stop the simulation as the amount of diffusion or tip streaming was causing the droplet shape to change (i.e. shrink) and the velocity ramp to respond to this false cue, incrementing the shear rate. For $M = 2.0$ (red plot) and $M = 3.0$ (green plot) the initial increase in the radius is ~ 2.0 lattice units before diffusion (or tip streaming) takes over; however the effect is small and the simulations run to completion. The effect on the Reynolds vs capillary number curves is demonstrated in figure 5.5. Note that according to equations 5.1 and 5.2,

$$Re(Ca) = \frac{\rho\sigma}{\nu^2} R.Ca \tag{5.7}$$

so that a change in the radius, R results in a change in the gradient of the Re vs Ca curve. Simulation parameters are given in section 4.3.1 for a viscosity of $\nu = 0.2362$. As the mobility is increased the plots correspond well.

5.3 Lattice size limitations

It was not possible to simulate to the point of break up droplet systems of high Reynolds number in the inviscid regime since the capillary numbers necessary required shear rates higher than achievable with the algorithm as it stands. At each time step the distribution functions cannot be propogated more than one lattice site and so the maximum velocity at the walls, $\dot{\gamma}L/2$ cannot exceed unity even ideally. However in practise this figure is nearer 0.2 after which instabilites lead to an abrupt halt to the simulation. For the system size being investigated (120×400) viscosities of less than or equal to 0.181 were unable to be simulated to breakup. It is hoped that in future a way round this premature termination of the relatively inviscid runs may be made by implementing a Lees-Edward based boundary condition [25]. This method 'cuts' the simulation up into a given number of smaller units which can then be set moving with a velocity v_{unit} with respect to each other; these can then be individually ramped up with velocity $\delta v << 1$ accessing higher shear rates and producing an overall simple shear profile.

Even though the computationally imposed limits on lattice width due to sheared walls may be resolved using this Lees-Edwards type boundary conditions the lattice size cannot increased without bounds. When placed in a sufficiently large system a fluid drop will dissolve due to free energy effects as discussed previously in section 5.2.4.

An important part of the current simulations is also to establish what effect the walls have: how do they influence the evolution towards or the dynamics of breakup? Tests performed on systems of dimensions 40×100 to 70×100 lattice units, all other parameters unchanged, show clearly how the close proximity of the walls seem to squeeze the drop towards the central line prematurely. Alignment with the central flow lines allow the drop to experience higher shear rates with very little deformation in response (see fig. 6.1). This effect will be observable experimentally when drops are sheared in narrow shear cells. Also important experimentally is how the periodic neighbouring drop affects the process of breakup since in experiments the neighbour is not present. Just how the walls influence break up will be discussed later (section 6.6).

Needless to say the optimal lattice size was chosen as 120×400 by considering overall lattice size, proximity of walls, influence of the periodic neighbouring drop, dissolution and computational efficiency.

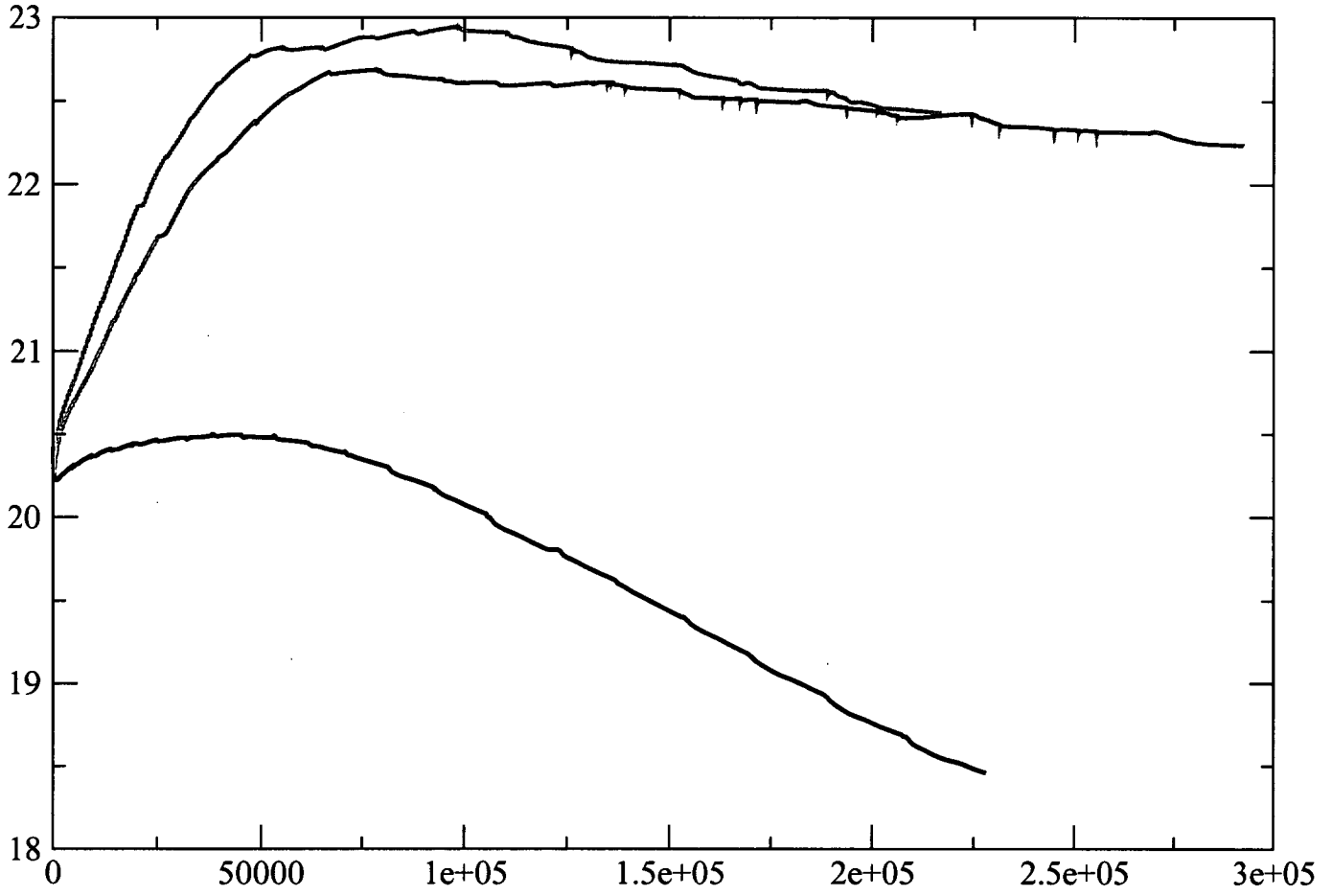

Figure 5.4: effect of mobility on drop radius: drop radius plotted against time for mobilities M=0.3 (black plot), M=2.0 (red plot) and M=3.0 (green plot). Viscosity $\nu = 0.2362$, lattice size 120 x 400, and initial shear rate increment $\Delta\dot{\gamma} = 1.66\text{x}10^{-4}$

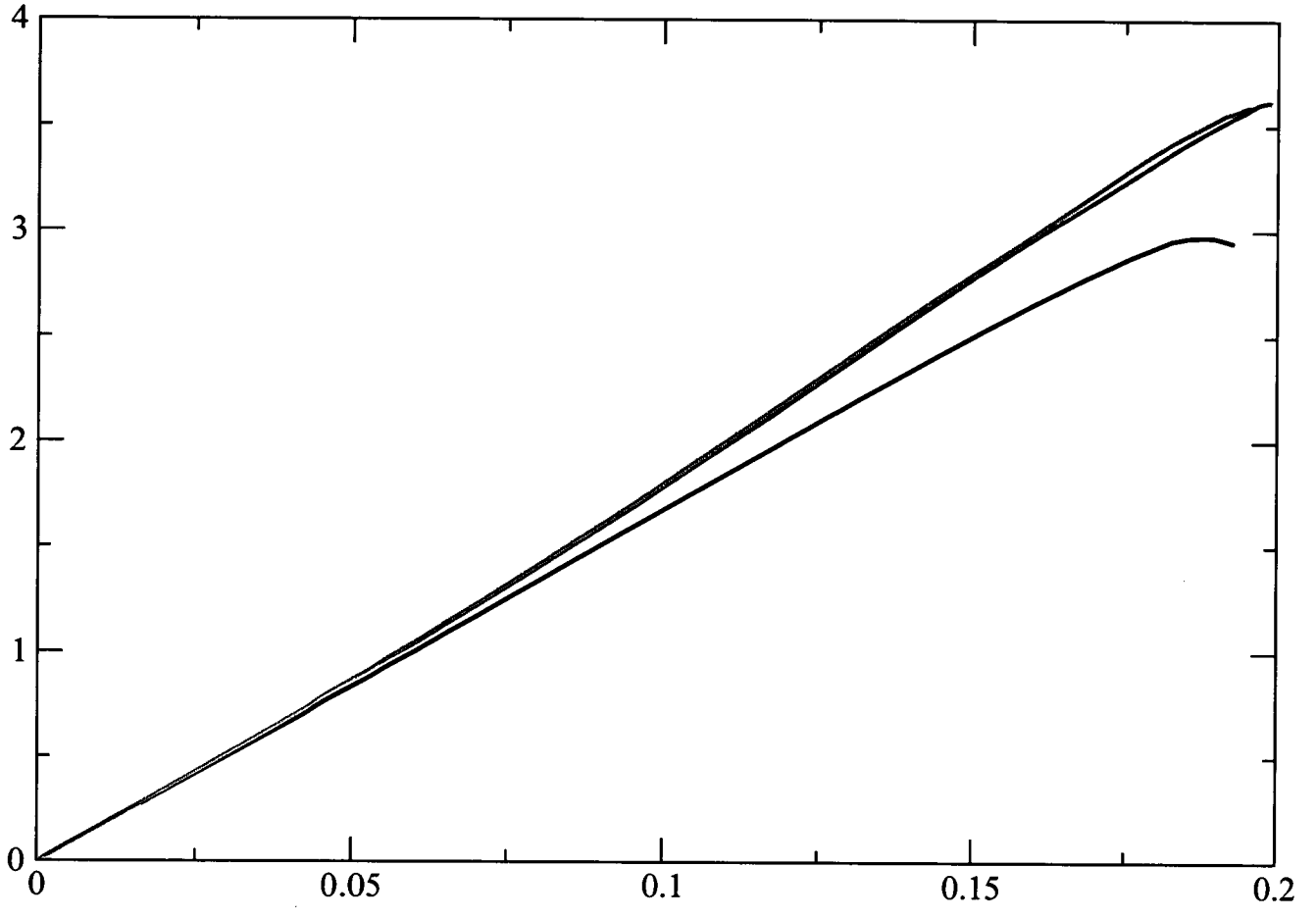

Figure 5.5: effect of mobility on Re vs Ca for mobilities M=0.3 (black plot), M=2.0 (red plot) and M=3.0 (green plot). Parameters are given in figure 5.4

Chapter 6

Results

6.1 Slow/Restricted Ramp

Take first the case where the drop is restricted to deform slowly, by steps in deformation, D (defined in equation 5.6) chosen to be no greater than 0.05. As the viscosity is increased from one run to the next (i.e. Reynolds number decreased) the capillary number required to achieve breakup steadily increases. Drops are rotated more and more towards the flow lines, where they will experience less shear (velocity gradient), withstand greater shear rates and attain higher deformations.

6.1.1 Morphologies

The parameters used for all the simulations presented here are specified in section 5.2.1 except where otherwise stated. A complete sequence of morphologies for the simulation of viscosity $\nu = 0.519$ is given in fig. 6.1. The direction of shear is given thus: $\uparrow\downarrow$. Save the final configuration, these are the stable shapes taken when the drop reaches equilibrium (by the criteria given is section 4.3) and prior to the next ramp increment. Initially ($t = 16451$) the deformation is slight ($D \sim 0.06$) with the major axis of the ellipse inclined about 48° from the horizontal axis. This is almost aligned with the principal axis of shear where the drop will experience maximum shear stress. At a time of $t = 105201$ the shape is notably elliptical with its major axis inclined $\sim 60^{\circ}$ to the horizontal axis. The next three morphologies show the ellipse flattening out at

the sides followed by an indentation developing and hence a two lobed structure. This concave indentation is then stretched out with the two lobes at the extremities persisting. At this point the drop has rotated round and is almost aligned with the flow lines. This appears to be approaching the final stable shape before breaking; the penultimate picture in this series showing the last stable three lobed state. As the ramp is further increased the refinements cannot be made small enough to allow a steady state and the final picture shows the drop as it continues to deform transiently and breakup. As it is stretched more the drop develops two concave indents (or necks) at the base of the extreme lobes and the central part 'bulges' out once more; the drop hence assumes a three lobed morphology on the point of breakup, as shown in the final picture in this series.

A similar sequence for the viscosity $\nu = 0.2362$ is shown in fig 6.2. Initially the evolution of the shape is very similar to the higher viscosity case shown in figure 6.1. However as the shear increment is refined the two lobed structure of the drop persists, stretches and the central region develops into a thin neck which eventually breaks. The last stable droplet is frame 6.2(e).

The final two pictures in this series show a non-stationary state which undergoing transient stretching before finally breaking up (the final picture shows the point of break up).

From the plots of deformation against capillary number (fig 6.7) and Reynolds number against capillary number (fig 6.8) it is evident that a sudden change in behaviour at the point of break up takes place. This is attested by the drop morphologies: note the two very different morphologies reached at the point of breakup for either end of the viscosity range simulated. For drops at the lower end of the viscosity range the morphology at the critical point below breakup is two lobed and deformations are moderate, about ~ 0.6, whilst drops at the higher end (about $\eta = 0.4$ and above) attain deformation of up to ~ 0.9 before breakup and have a three lobed structure with a large central body and two smaller lobes at either extremity.

Any curvature once it has developed in the structure, possibly due to the Laplace pressure, might be expected to lead to an unstable structure. However the observed behaviour that concavities are present in steady state indicate that the process is more complicated. The shear forces and stresses acting on the droplet presumably stabilise these indents. Small changes in shear rate hereafter will instigate a process of transient stretching and breakup. It is interesting to note that an imposed shear flow has been found to stabilise a two dimensional lamellar domain by advecting the top and bottom interfaces with respect to one another; this displacement means

they cannot maintain the exact phase relation that would lead to pinch off due to the Laplace pressure [7].

6.1.2 Velocity Maps

It is instructive to look in detail at the velocity maps of the above two and three lobed structures once they have reached equilibrium and before breakup. That the shape has reached equilibrium will be apparent from the velocity vectors which will be everywhere parallel to the interface. Velocity maps of the above structures show that initially for spherical and elliptical morphologies the flow inside the drop is that of a single vortex, with the velocity vectors parallel to the interface everywhere when it reaches a steady state. Fig 6.3 shows the velocity map for inside an elliptical drop. As the structures become two lobed and have a central negative curvature it may be possible that a vortex is present in each lobe. Figure 6.4 shows the central section of a velocity map from a two lobed morphology. Clearly visible are the ends of two vortical 'swirls'. How these vortices influence the drop breakup is uncertain, however it may be that they somehow drag the interfaces together close enough that a pinch off occurs.

A velocity map of an elliptical droplet, viscosity= 0.181, with the shear profile subtracted shows the direction of the velocity acting to regain a spherical shape i.e. velocity vectors pointing inward at the tips and outward at the flatter sides (fig. 6.5). However this is for one of the lowest viscosities used and in simulations this run could not be taken to the point of breakup due to instabilities arising (see section 5.2). This can be compared with a similar map for Stokes flow in section 6.3. Still, using the same example and looking at the central portion of the drop with the whole velocity field displayed, there already appears to be the development of two vortices in this elliptical structure (fig. 6.6).

6.1.3 Deformation vs capillary number curves

Plots of D vs Ca show distinctly the change in behaviour (fig 6.7). At small capillary numbers and hence small deformations, runs of all viscosities have a linear dependence of D on the shear

a) T=16451$\dot{\gamma} = 0.000168$

b) T=47401 $\dot{\gamma} = 0.000420$

c) T=105201 $\dot{\gamma} = 0.000756$

d) T=506501, $\dot{\gamma} = 0.001155$

e) T=955701, $\dot{\gamma} = 0.001239$

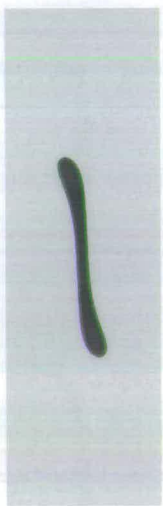

f) T=1368601, $\dot{\gamma} = 0.001450$

g) T=1608801,$\dot{\gamma} = 0.001702$

h) T=1661851,$\dot{\gamma} = 0.001807$

i) T=1738301, $\dot{\gamma} = 0.002332$

Figure 6.1: evolution of morphologies during 'restricted' ramping of $\nu = 0.519$

a) T=13771 $\dot{\gamma} = 0.0005084746$

b) T=56356 $\dot{\gamma} = 0.0011864407$

c) T=90220 $\dot{\gamma} = 0.0014406780$

d) T=119239 $\dot{\gamma} = 0.0015254237$

e) T=261376 $\dot{\gamma} = 0.0017161017$

f) T=316405 $\dot{\gamma} = 0.0017319915$

g) T=final, point of breakup

Figure 6.2: evolution of morphologies during 'restricted' ramping of $\nu = 0.2362$

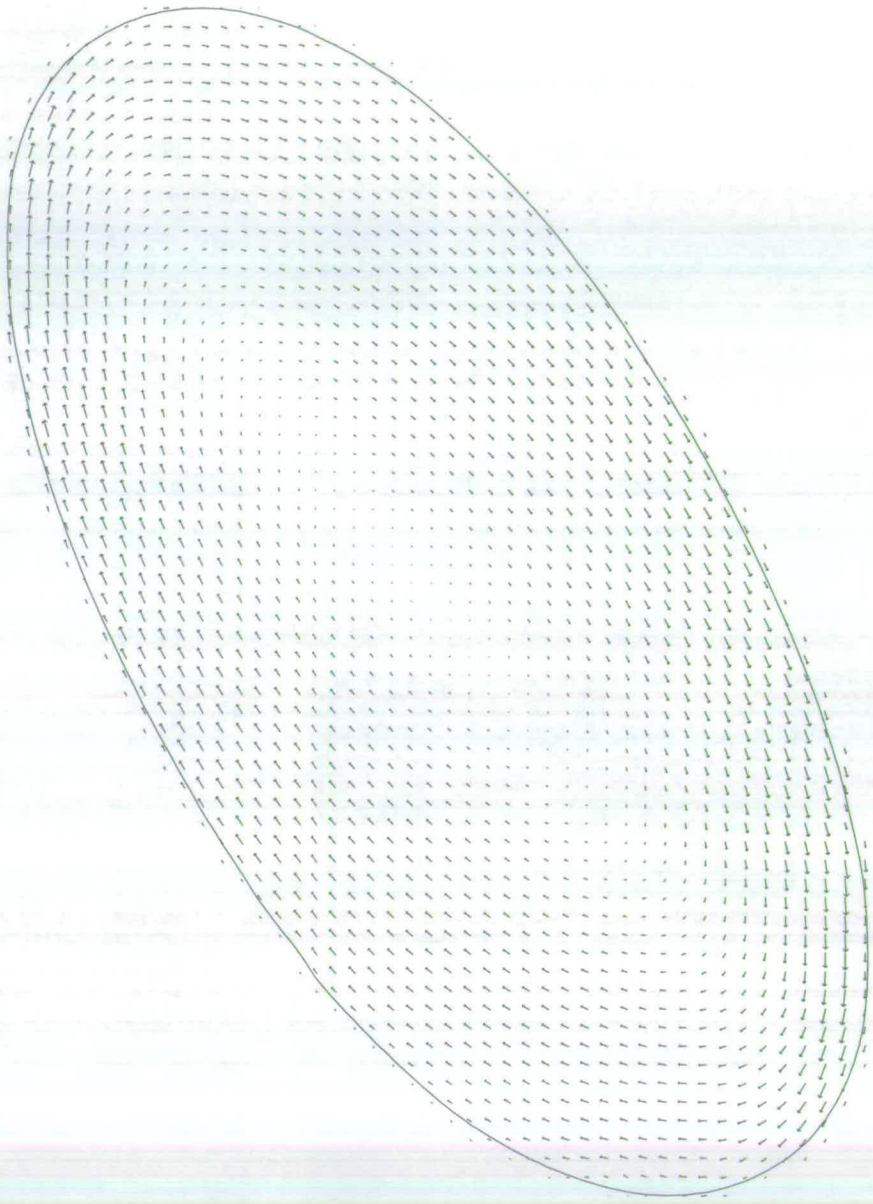

Figure 6.3: velocity map of interior of ellipse, viscosity= 0.519. Taken from figure 6.1c. Drop width taken tip to tip is 46 lattice units. The maximum velocity shown in the ellipse is $u = 0.0098$ whereas the velocity near the walls is $u = 0.0448$

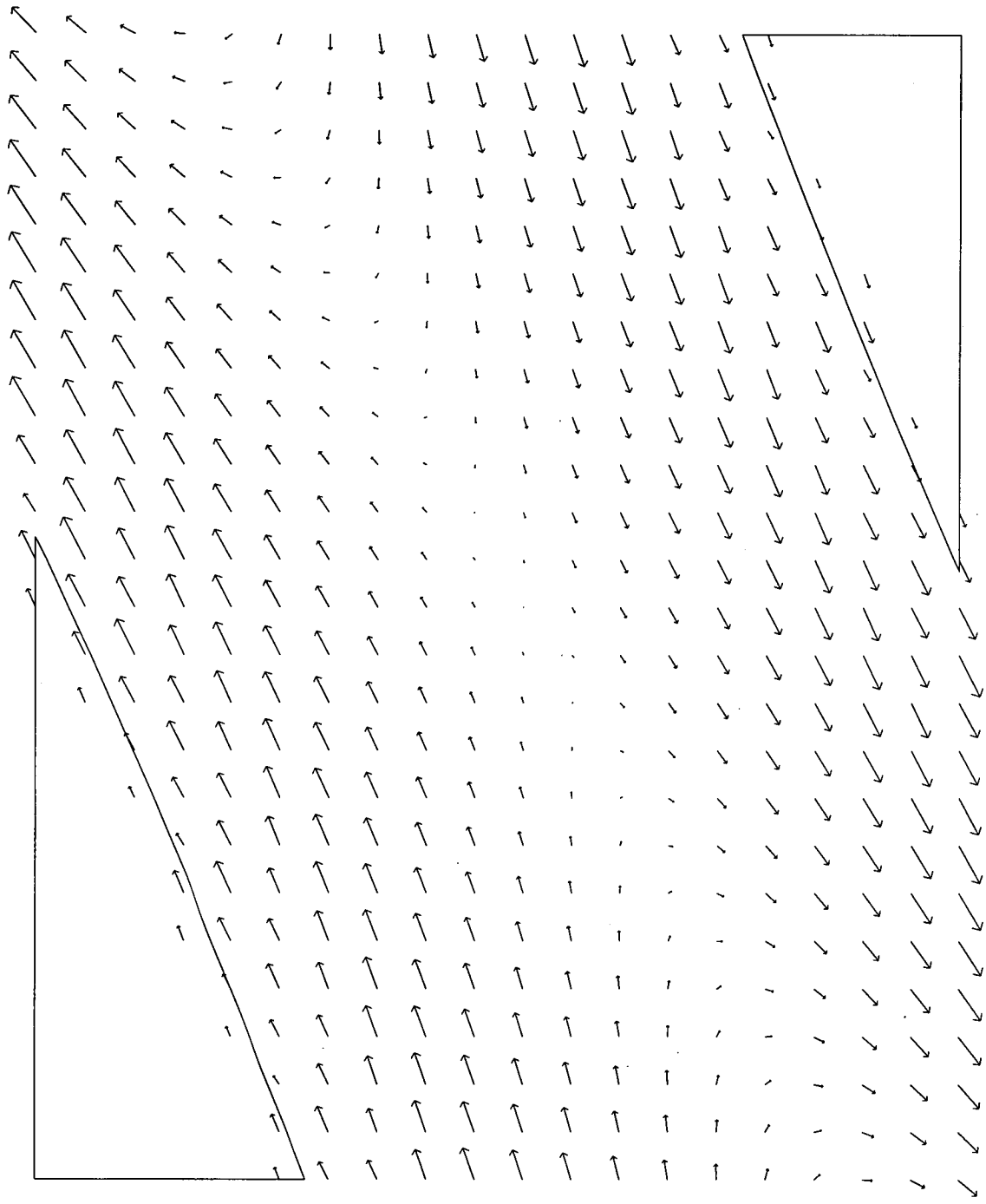

Figure 6.4: velocity map of central portion of drop showing two vortices. Figure taken from fig 6.2e. Maximum velocity vector shown gives $u_{max} = 0.006$.

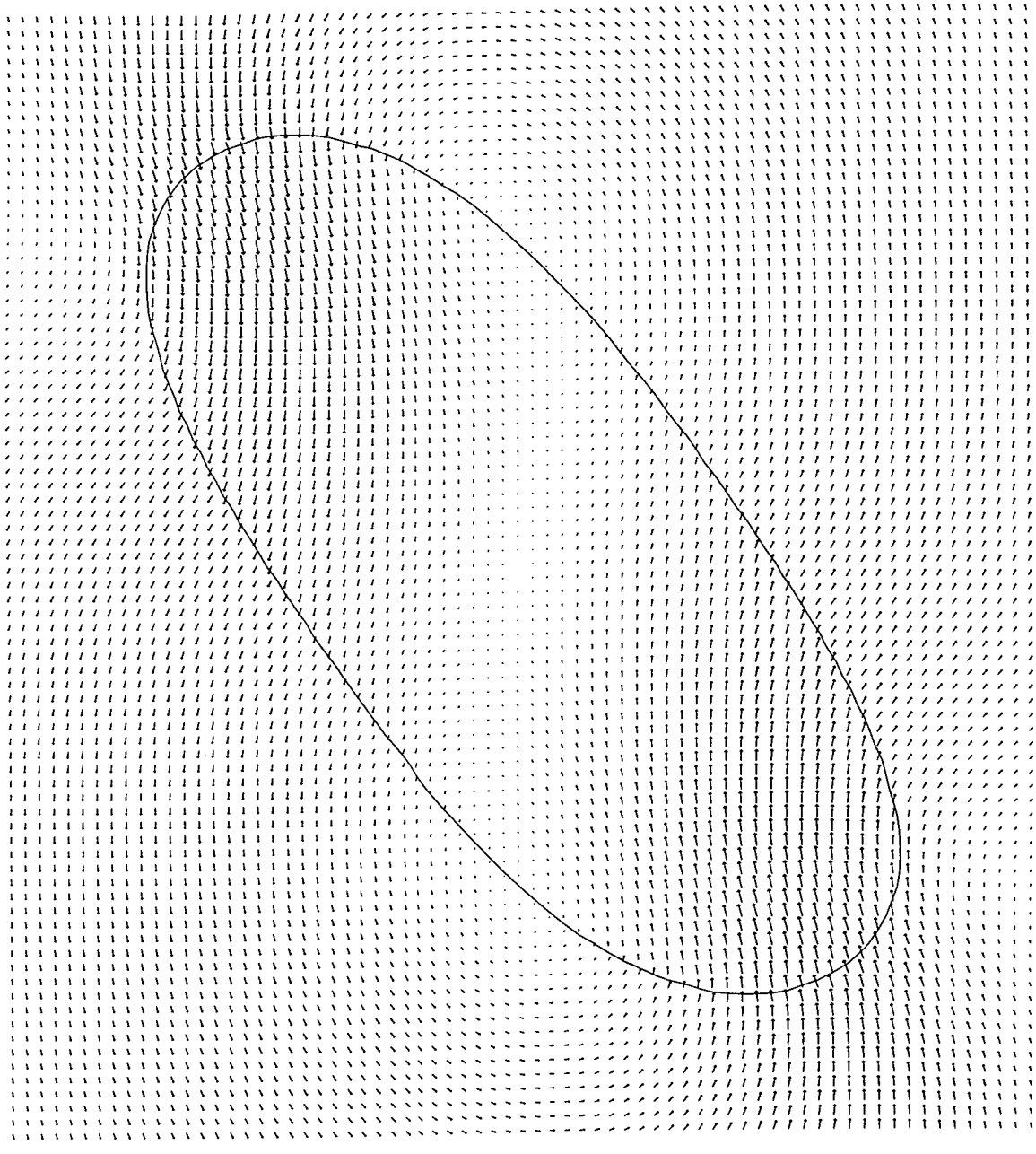

Figure 6.5: velocity map with shear profile subtracted of ellipse viscosity= 0.181. Shear rate at this instant is $\dot{\gamma} = 0.00175$. Ratio of drop (tip to tip) width/wall separation is 26/52.

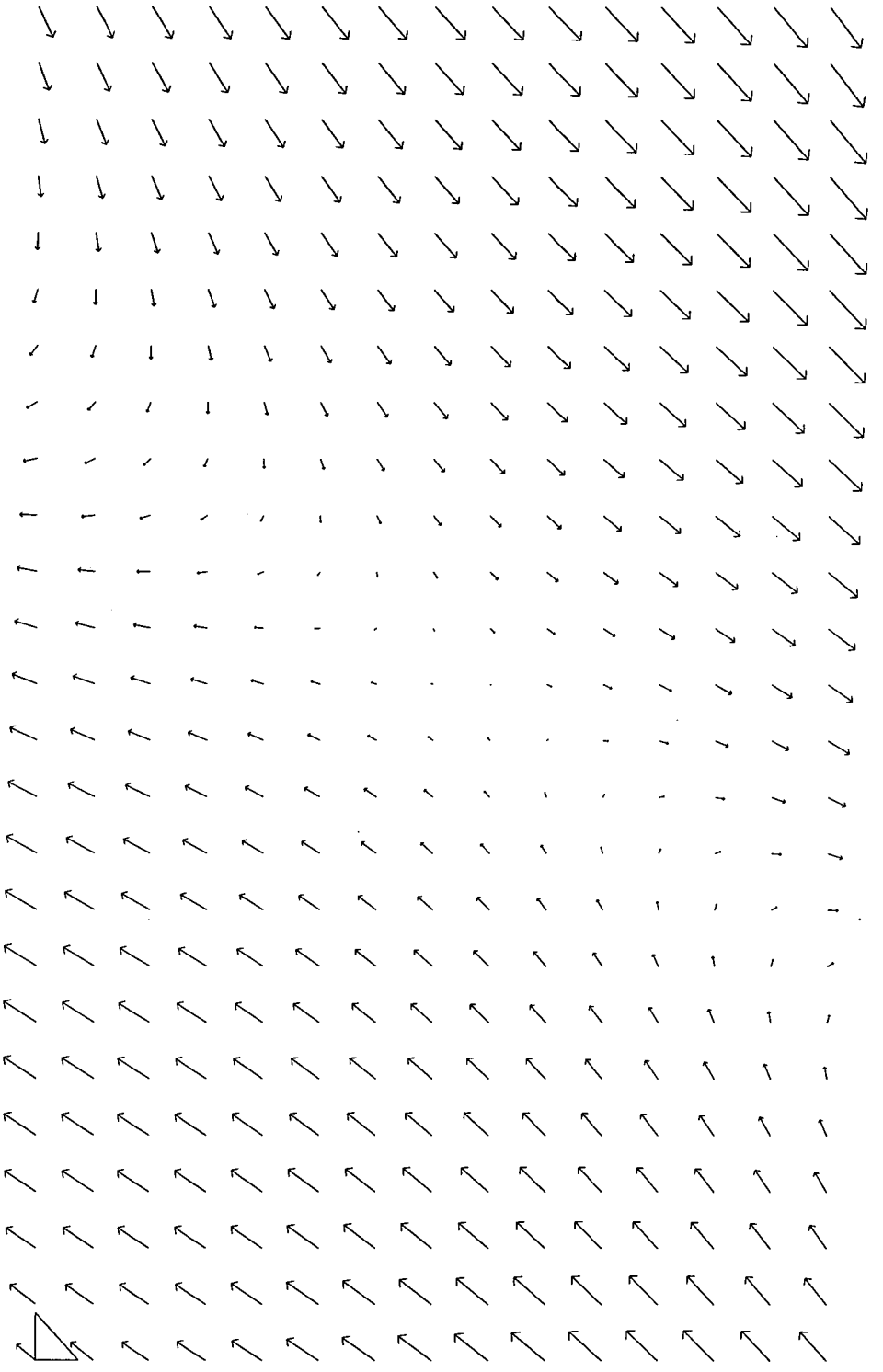

Figure 6.6: velocity map showing possible vorticity in elliptical structure viscosity= 0.181. The size of this frame is 15 x 25 lattice units and is obtained by magnifying central section of fig.6.5

rate. Here the drop is aspherical but only slightly elliptical. As the capillary number increases the linear dependence no longer holds and the plot now curves upward; a larger deformation is induced in response to an increase in shear. There comes a point where the curve steepens sharply and small changes in Ca give rise to very large changes in deformation. At this point the drop shape is now a 'stretched' ellipse and the sides develop a concave indentation. Beyond this point for the lower viscosities, the drop will break. However the larger viscosities are somehow insensitive to this apparent instability and go on deforming; the plots eventually develop a 'flat tail' where large increases in Ca produce very little change in deformation. At this point the drops have rotated towards the flow lines and experience minimum velocity gradients and a three lobed structure has formed. Runs with these viscosities are insensitive to the instability in the two lobed form. This insusceptibility leads them to 'jump over' the instability, accessing another stable regime by assuming the three lobed form. It should be noted that the plot on the far left of the diagram for the least viscous run did not run to completion due to instabilities in the simulation (see section 5.2) and is included only to confirm the overall trend.

6.1.4 Reynolds number vs capillary number curves

It is also useful to depict the results in a Reynolds number vs capillary number space (fig 6.8). In this plot the curves are very nearly straight lines because both Re and Ca are linear in the shear rate $\dot{\gamma}$. The small deviations from linear are due to the non constant volume of the drop (see section 5.1.3) which lead to a small change in R_0. It is essential, however, that the length scale used in calculating the Reynolds and capillary number is derived from the true volume at the current value of shear rate (and not from the initial droplet volume before evaporation) if the plots are to show anything useful. From these plots it is clear to see when diffusion is large and the results cannot be trusted; a marked downward curving of the graph is apparent and usually precedes total dissolution and the premature termination of the simulation. Such data is excluded from the figures in this section. The endpoint of the remaining plots marks the critical capillary number beyond which no stable shape (under the conditions stated previously) exists. Again it should be noted that the plot on the far left of the diagram for the least viscous run did not run to completion due to instabilities in the simulation (see section 5.3) and is included

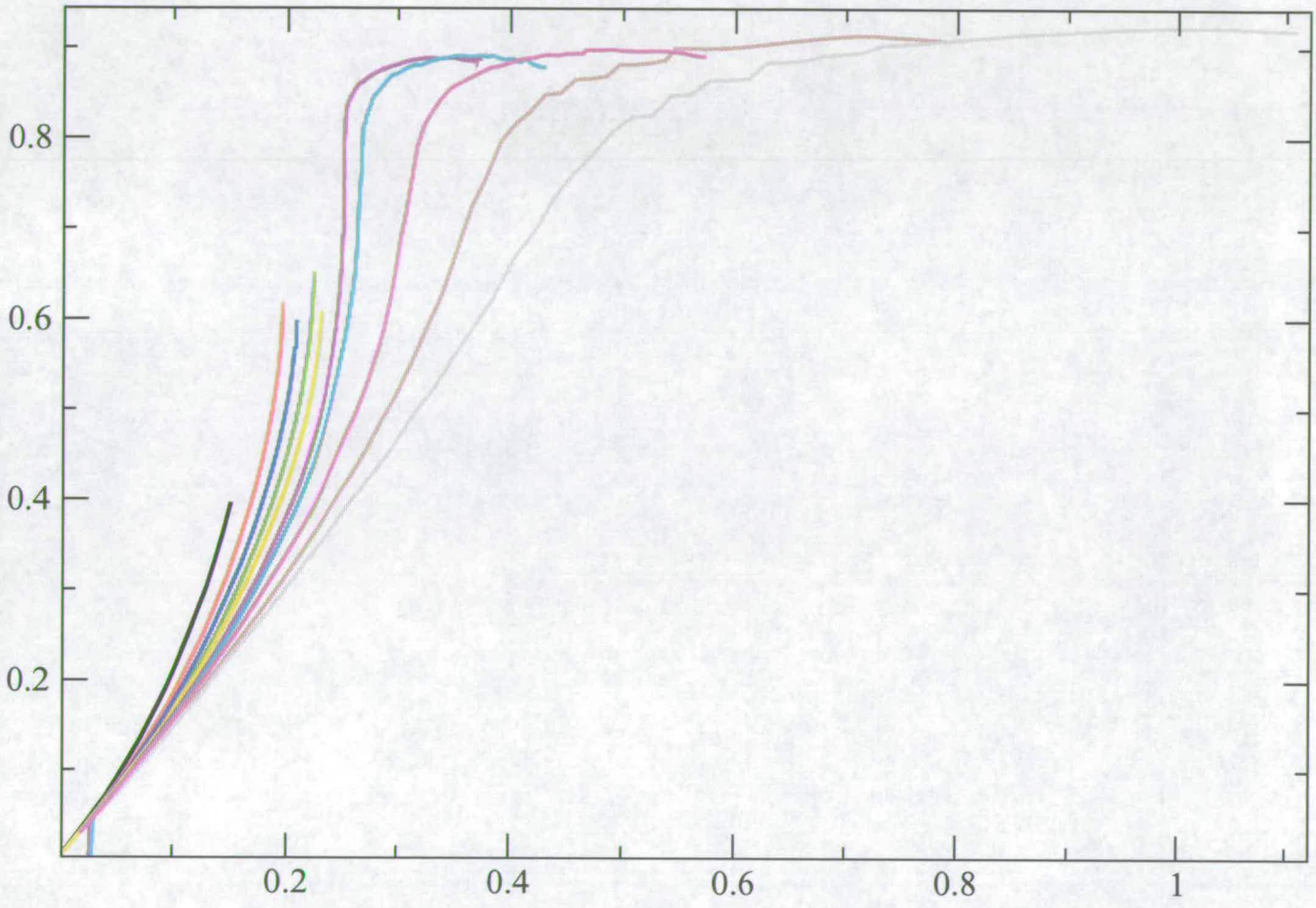

Figure 6.7: D vs Ca curves for restricted ramp. Viscosities increase from left to right.

only to confirm the overall trend. From the leftmost to the rightmost run shown, the viscosity increases.

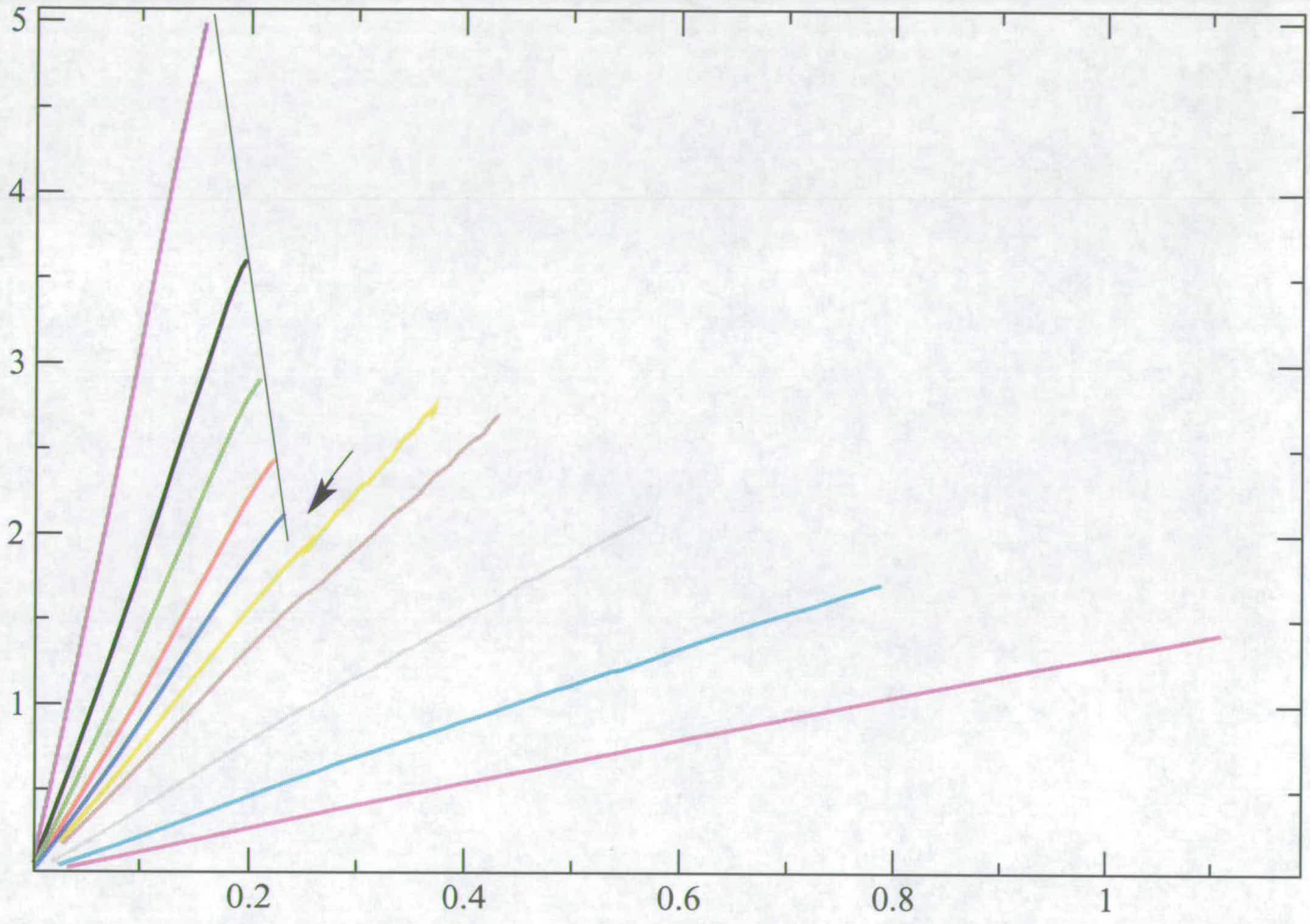

Figure 6.8: Re vs Ca curves for restricted ramp. Viscosities increase from left to right. Note colours may vary from previous plot.

The black line drawn on the plot marks a boundary where the lower viscosity runs become unstable according to the criteria in section 4.3 and a small enough ramp increment cannot be found to allow the drop to deform 'slowly'. These all share the common morphology of a two lobed structure. As the viscosity is increased the deformation of the drops increases slightly as does their orientation towards the flow lines ($65 - 68^o$). Increasing the viscosity further results in the orientation of the drops reaching $85 - 88^o$, i.e. more or less aligned in the flow direction, and further deformation is minimal in response to increased shear. Correspondingly the drops evolve into three lobed structures, that would ultimately break if the ramp where continued, into three. This is evident in the plots from the increase in capillary number required to break drops of higher viscosity. However for a viscosity of $\nu = 0.367$, corresponding to the yellow plot both final morphologies have been obtained in separate runs. This is probably due to some change in initial conditions or possibly the size of the initial ramp increment, however it indicates that this set of parameters must lie very close to the transistion. The arrow on figure 6.8 marks a transition point between two and three lobed structures, where an abrupt alteration in the Reynolds and capillary number values at breakup is produced on varying the viscosity.

6.2 Fast/Unrestricted Ramp

The above data was intended to represent a situation where the shear rate is increased arbitrarily slowly until droplet breakup occurs (slow ramp). Using the same parameters as above the simulations are performed again, this time with the restriction on the deformation lifted: in response to an increase in shear the drops are allowed to deform unconstrained (see section 4.3 for details). Very different behaviour is now observed for the lower viscosities at the critical point before breakup.

6.2.1 Morphologies

With the restriction on the deformation in response to shear lifted the critical point morphology of the drops is one of three lobes for all of the viscosities simulated and the sequence of formation similar to the case shown in figure 6.1. At the end point a more or less constant deformation is reached, $D \sim 0.9$. Increasing the viscosity again causes an increase in the capillary

number to achieve breakup. Orientations range from $85 - 88^{o}$ as with the higher viscosities in the restricted ramp case. It is possible that with the lower viscosities this method of ramping is not sufficiently slow to detect the instability of the two lobed structures, consequently they pass through this phase into another regime of stable or metastable three lobed structures.

6.2.2 Velocity Maps

Velocity maps were examined but showed no significant differences from those of similar droplet morphologies obtained by the restricted ramp.

6.2.3 Deformation vs capillary number curves

Looking now at plots of D vs Ca (fig. 6.9) it is seen that the behaviour is different from the slow ramp, particularly in the lower viscosity runs. As with the other plots all viscosities are initially linear for small deformations and shear rates. The plots then curve upward to the point where they are almost vertical and a small increase in capillary number produces a large increase in deformation. Beyond this threshold, runs for all viscosities reach a similar deformation and develop a long flat tail in the Re(Ca) curve where large increases in capillary number give little change in deformation. This corresponds to the three lobed shape seen in the morphologies above. They have rotated round to the vertical where the shear stress will be minimum.

6.2.4 Reynolds number vs capillary number curves

From the plot of Re vs Ca (fig 6.10) it is clear that there is no sudden change in breakup behaviour and morphology upon increasing viscosity as was the case when the deformation was restricted.

Instead of there being two distinct trends in the endpoints, particularly between the relatively lower and higher viscosity runs these plots 'fan' out, attesting to the observation of a three lobed structure at breakup throughout.

It is clearly seen here that all runs reach about the same deformation at the critical point. Similar to the 'restricted' case, the critical capillary number beyond which no stable shape exists,

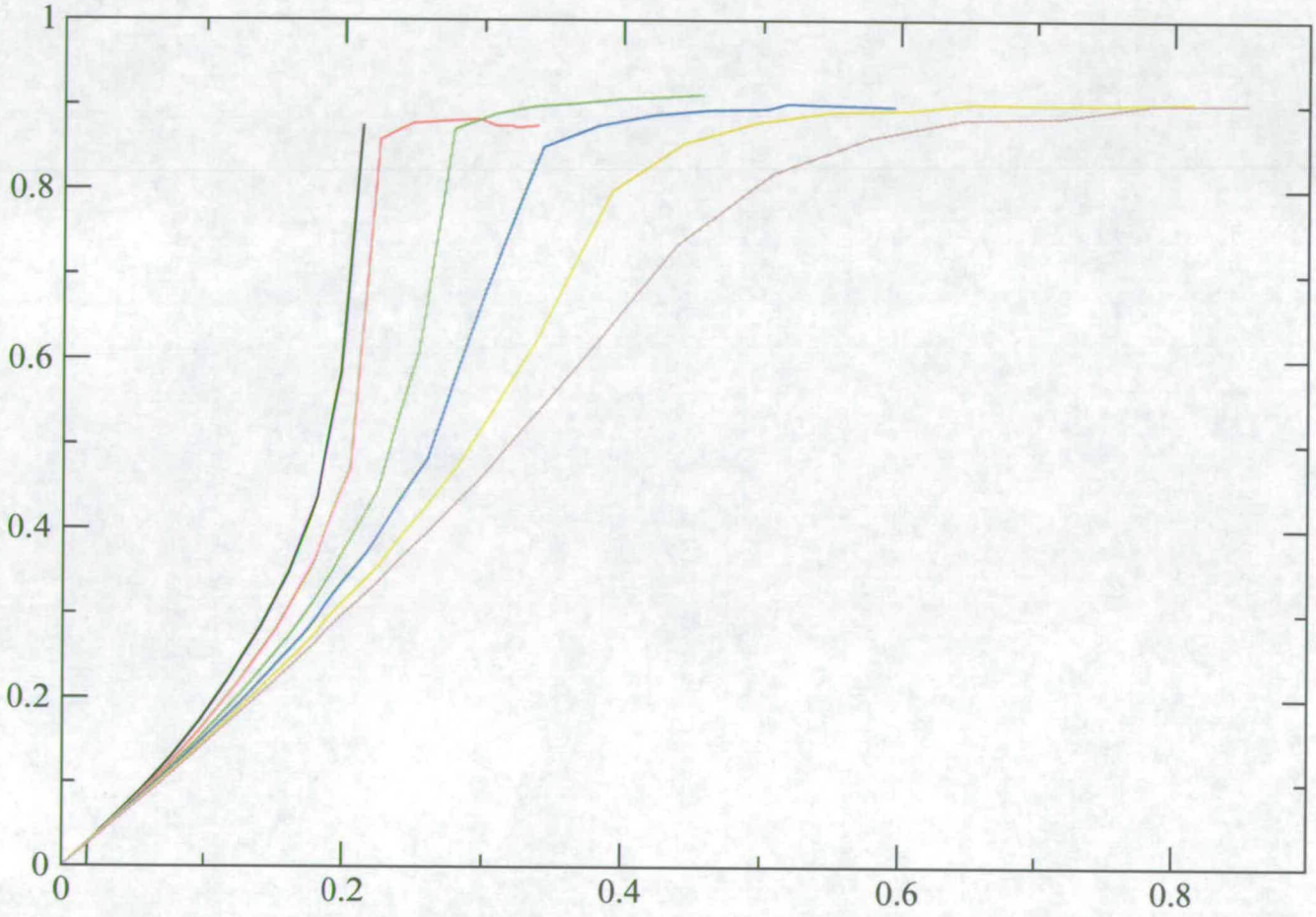

Figure 6.9: D vs Ca curves for unrestricted ramp. Viscosity increases from left to right. Plots correspond to parameter sets for runs 1, 2, 3, 4, 5, 6 as given in section 5.2.1.

increases with the viscosity. That these three lobed 'metastable' shapes in the lower viscosity runs exist beyond the endpoints reached in the 'slow' ramp indicates that the method of ramping or the time history of the flow has a large influence on the manner of breakup.

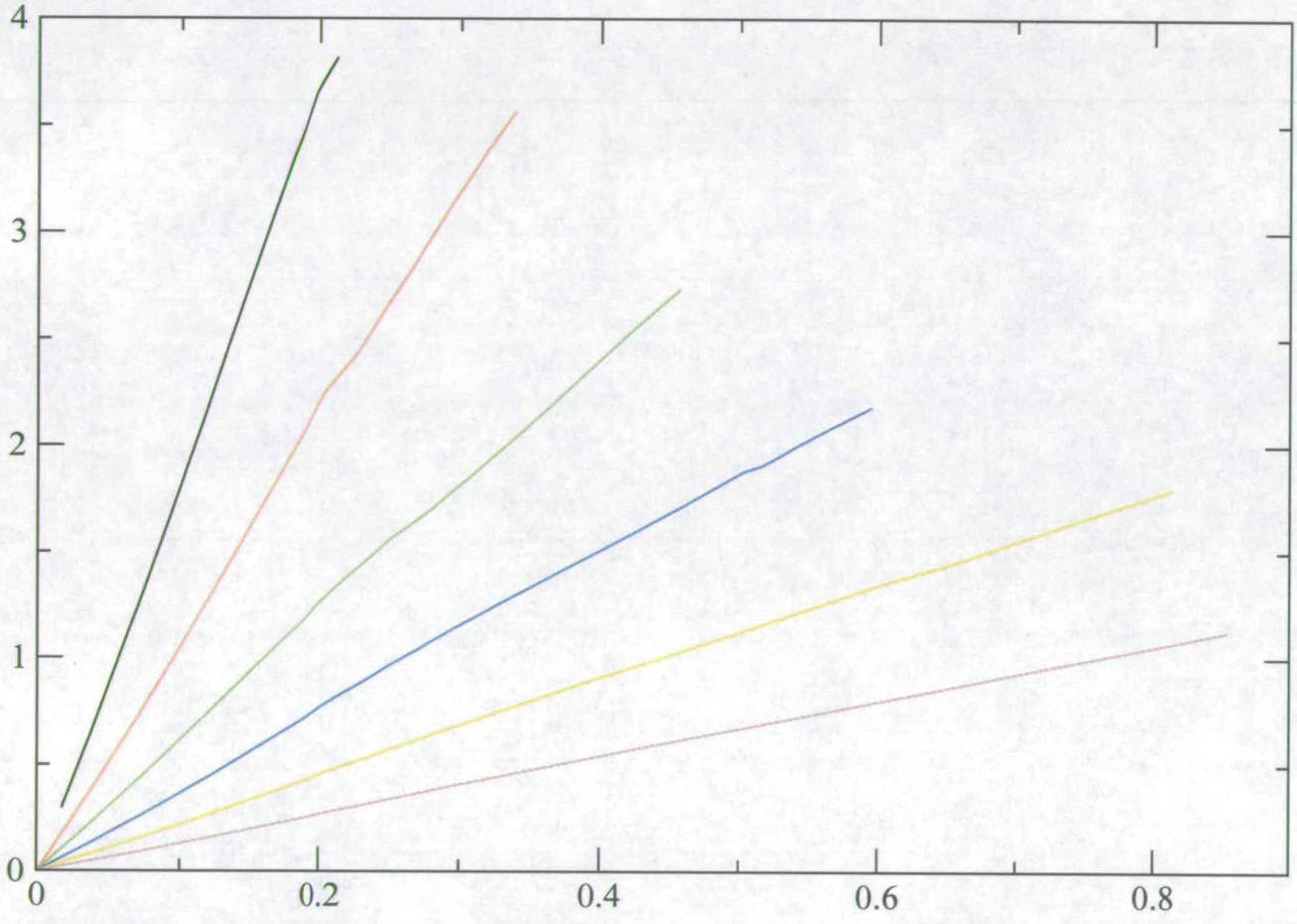

Figure 6.10: Re vs Ca curves for unrestricted ramp. Parameters as given in fig 6.9.

6.3 Zero Reynolds Number

To access the limiting case of zero Reynolds number, simulations of Stokes flow were performed. This is achieved by commenting out the non linear term of the Navier Stokes equation in the Ludwig code (i.e. setting $\mathbf{u}.\nabla\mathbf{u} = 0$ in eq. 3.15) and waiting for a steady state to be achieved in which $\dot{\mathbf{u}} = 0$.

Since this then renders the equation determining the velocities linear it is possible to look at a map of the velocity generated by the interface stress alone. Taking an elliptical shape near the beginning of the simulation the shear flow contribution to the velocity is subtracted and the result is shown in figure 6.11.

It is evident from this that the motion of the interface is acting to regain a spherical shape and thus generates a flow with velocity vectors pointing inward at the tips of the drop and outward and the flatter sides.

Shown in figure 6.12 are plots of deformation vs capillary number, the rightmost D(Ca) curve being the results from the Stokes flow simulation. The previous D vs Ca data for slow ramps (fig 6.7) is included for comparison. The Stokes result is consistent with the trend established previously.

Figure 6.13 shows the morphology near the end of the Stokes flow simulation. The drop has rotated until parallel with the flow lines, becoming extremely long and slender; it is now only 5-6 lattice nodes across with the sides showing very little curvature, if any. This suggests that in the limit of zero Reynolds number there exists no hydrodynamic breakup mechanism. Stretching is proposed to continue until ultimately the drop is so thin that 'breakup' due to the intervention of a non-hydrodynamic (diffusive) mechanism results. With a morphology this elongated, the influence of the periodic neighbour can not be ruled out. It is not known whether this interaction (which could only be avoided by way of extremely large system sizes) will hinder or promote a non hydrodynamic breakup.

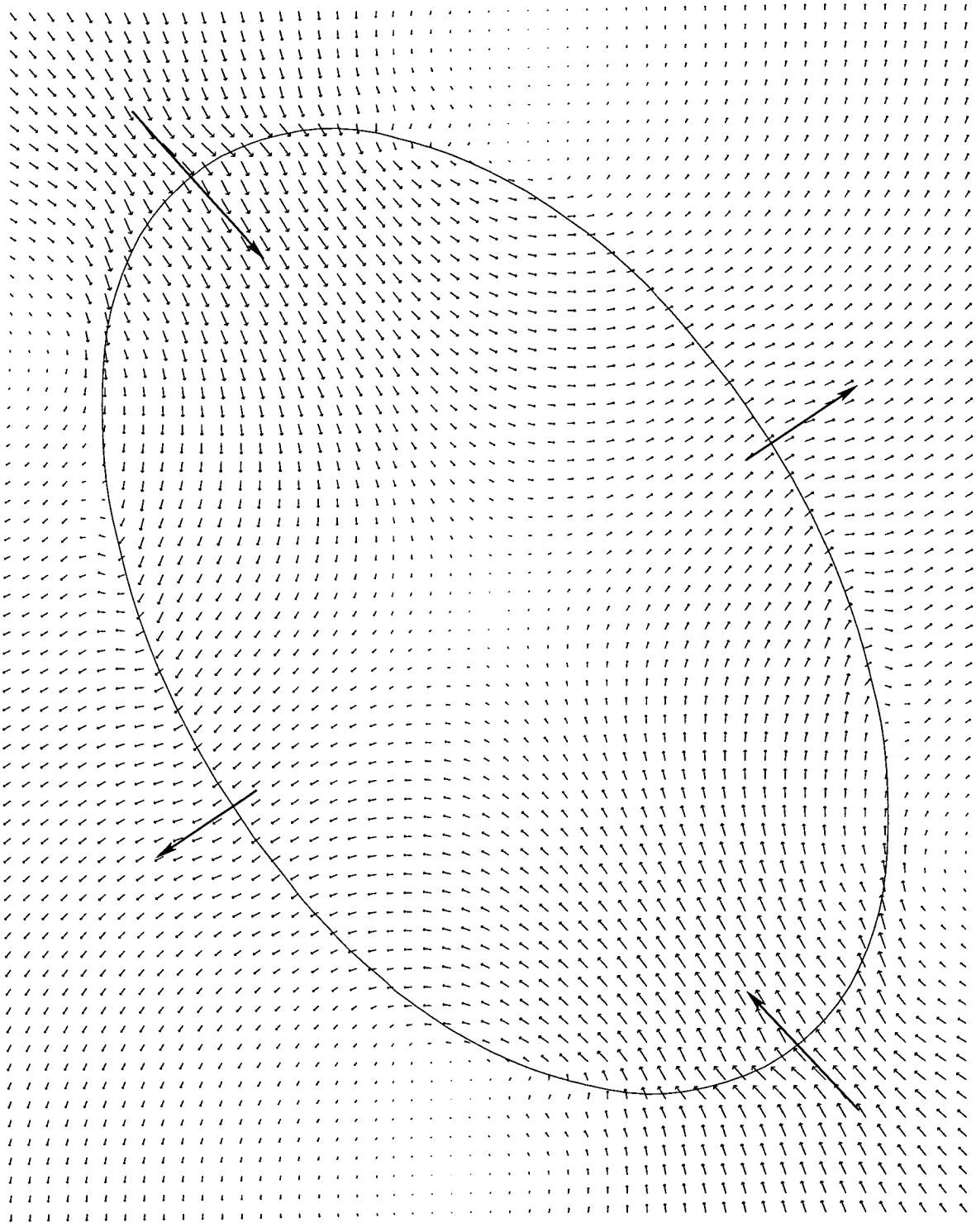

Figure 6.11: stokes flow: velocity map of ellipse with shear flow subtracted. The shear rate at this instant is $\dot{\gamma} = 8.47x10^{-4}$. Ratio of drop (tip to tip) width/wall separation is 21/60. Note full velocity field shows only a single vortice inside drop.

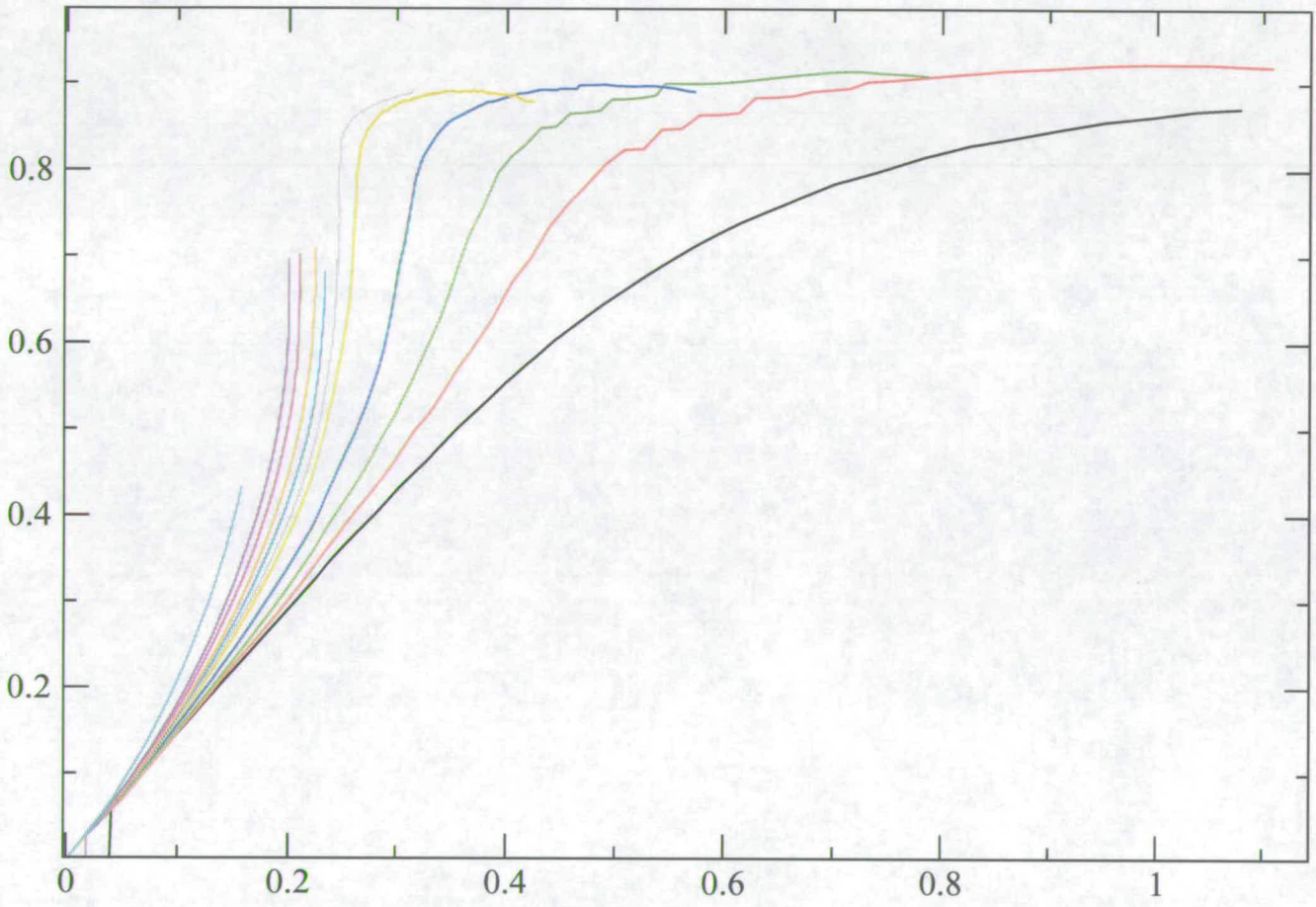

Figure 6.12: D vs Ca curves for restricted ramp. Lowest curve represents Stokes flow; remaining curves are as in fig. 6.7

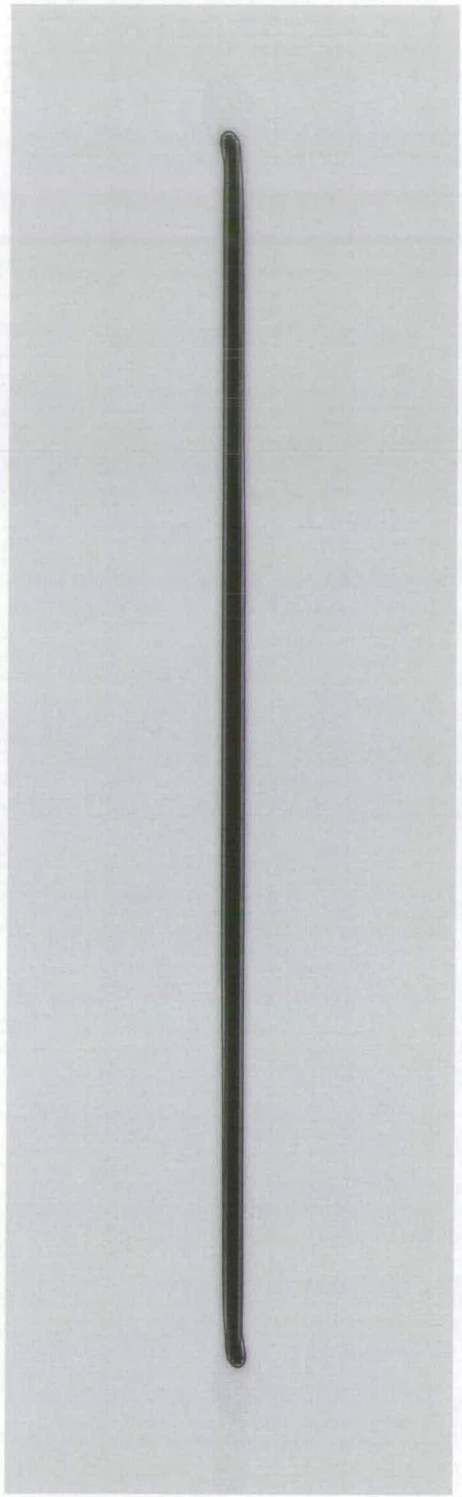

Figure 6.13: Final morphology from Stokes flow simulation

6.4 Comparison with 3d case

There appears to be no directly similar studies into the role of inertia in drop breakup in 3 dimensions; however given the difficulty of the problem this is not surprising. There is at least one study into the effect of inertia but not using the type of ramp constructed here [19]. It could possibly be conjectured that a similar study in 3 dimensions would always produce a two lobed breakup morphology as the viscosity is increased. However it is uncertain how the walls would now influence the results. Finite size effects in the third dimension are not anticipated to play a significant role.

However, the results here show some extremely elongated and stable morphologies in 2 dimensions. This is not envisaged to be the case in 3 dimensions. Such 'dimples' as are produced here in 2 dimensional structures would in 3 dimensions produce a strong inward force due to the Laplace pressure. Lord Rayleigh's investigation as to the instability of a cylinder of fluid shows that perturbations of wavelength $\lambda = 9r$, where r is the radius of the cylinder, grow fastest and lead to breakup and so the fluid collects in energetically favourable spherical drops [15]. As the neck thins the second radius of curvature becomes infinite and induces drop breakup. This hydrodynamic mechanism of breakup is thought to always to be present in 3 dimensions – as opposed to diffusive mechanisms which may ultimately control breakup in 2 dimensions, at least at low Reynolds numbers. In particular, the analogue of fig 6.13 in 3 dimensions could not exist due to the Rayleigh instability.

6.5 Consistency checks

It is important to keep in mind that all the plots and graphs shown above account for the non-constant volume of the drop by using a measure of the current droplet volume (at any given shear rate) to extract the length scale used. If this is not done the curves do not collapse. Also it is desirable that the results are independent of the simulation details, for example the lattice size.

6.5.1 Tests on smaller lattices

The lattice size used above is a scaled up version of a smaller lattice that has been initially investigated. Parameters are scaled so as to keep the Re/Ca ratio the same i.e. on increasing lattice dimensions by a factor 2, the relevant length scales obey $L \rightarrow 2L$ and the viscosity $\nu \rightarrow \sqrt{\nu}$. (The length scales required to be scaled are the drop radius and the 'width' of the lattice.)

Using the results from smaller lattices the effects of lattice size are also investigated. These simulations were done using a 'continuous' ramp with shear rate increment of 8.47×10^{-9}. By continuous it is meant that the ramp is increased every time step. The shear increment was established by running test simulations with different shear rates until a threshold amount was found, below which the results converged. Previous runs had given this as the maximum increase possible. Parameters used were surface tension 0.0456, viscosity 0.167, and the mobility 3.0. Below are Reynolds number vs capillary number (fig. 6.14) and deformation vs capillary number (fig 6.15) plots for various lattice sizes: blue 60×75, red 60×100, green 60×200, black 40×100, yellow 70×100.

In the Re vs Ca plots (fig 6.14) the increased diffusion experienced in the larger lattices is shown by the hooked end of the curves and is too great to be corrected by proper length scaling (see section 5.1.3). The 60×100, 60×200, 70×100 lattices, apart from the marked diffusive effects in the larger lattices at the end of the simulation, all give a good convergence of data. These results show that extending our data on droplet breakup to very large lattices would not be practical without a more fundamental way of preventing evaporation. As discussed in section 5.2.4, an attempt to control evaporation is made by setting to mobility to as high a value as is computationally stable, which, for these simulations is 3.0, the same value as for the data presented previously.

It is likely that wall effects come into play in the 40×100 simulation. The Re vs Ca (fig 6.14) plot of this lattice size extends far beyond the others reflecting the three lobed structure the drop assumes; as does the D vs Ca (fig 6.15) plot which shows a long flat tail where an increase in Ca produces very little deformation unlike simulations on lattices with a greater width or x dimension.

Figure 6.16 demonstrates the influence of lattice length and, therefore, periodic neighbour on the final morphology. The LHS lattice is 40×200 whilst the RHS lattice is 40×100 for

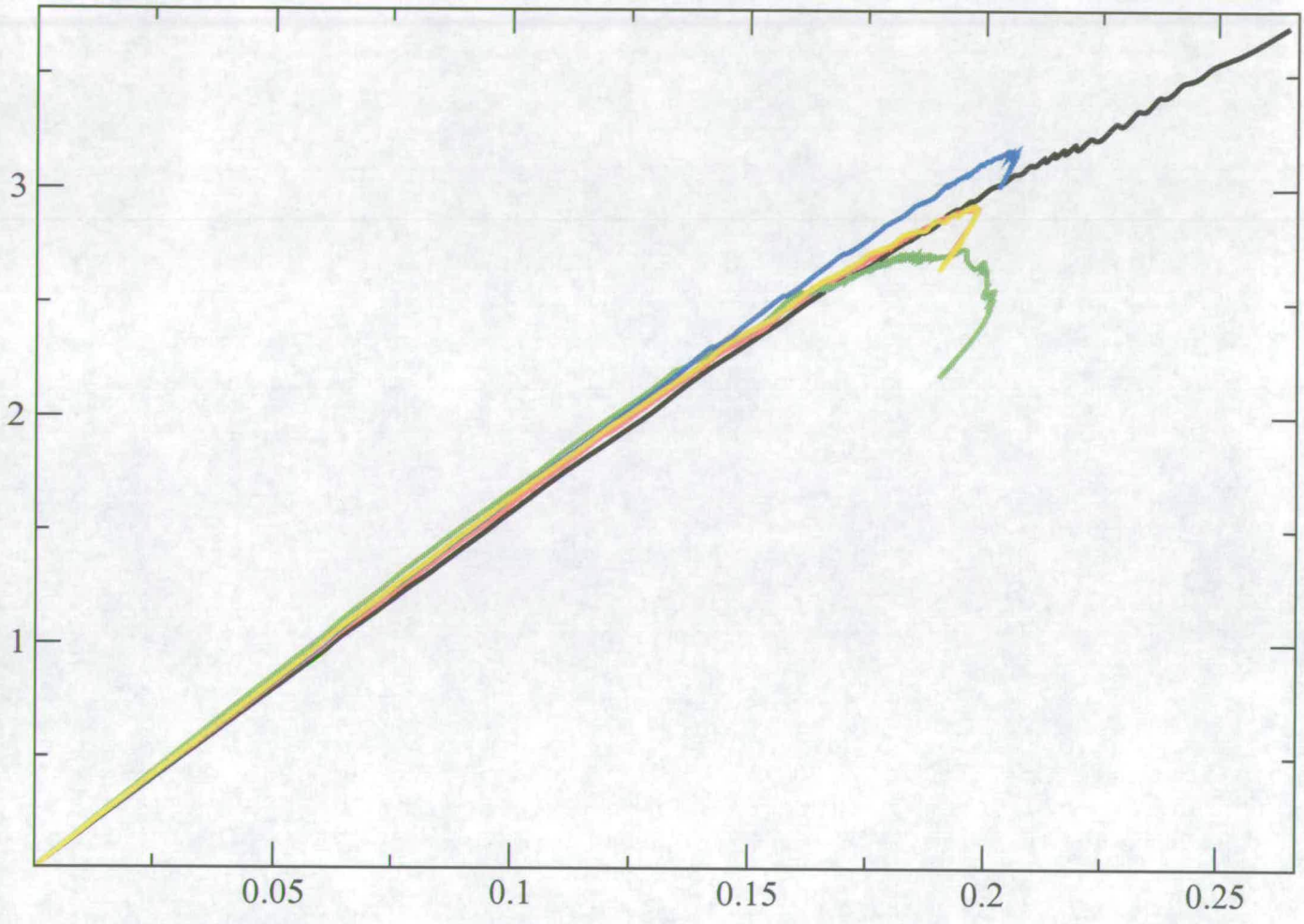

Figure 6.14: Effects of lattice size tested on smaller lattice on Re vs Ca. Lattice sizes are 60 x 75 (blue plot), 60 x 100 (red plot), 60 x 200 (green plot), 40 x 100 (black plot), 70 x 100 (yellow plot). The viscosity is $\nu = 0.167$, the shear rate increment is $\Delta\dot{\gamma} = 8.47x10^{-9}$ and is increased every time step. The final shear rate before plots diverge (corresponding to $Ca = 0.151$) is $\dot{\gamma} = 4.35x10^{-3}$

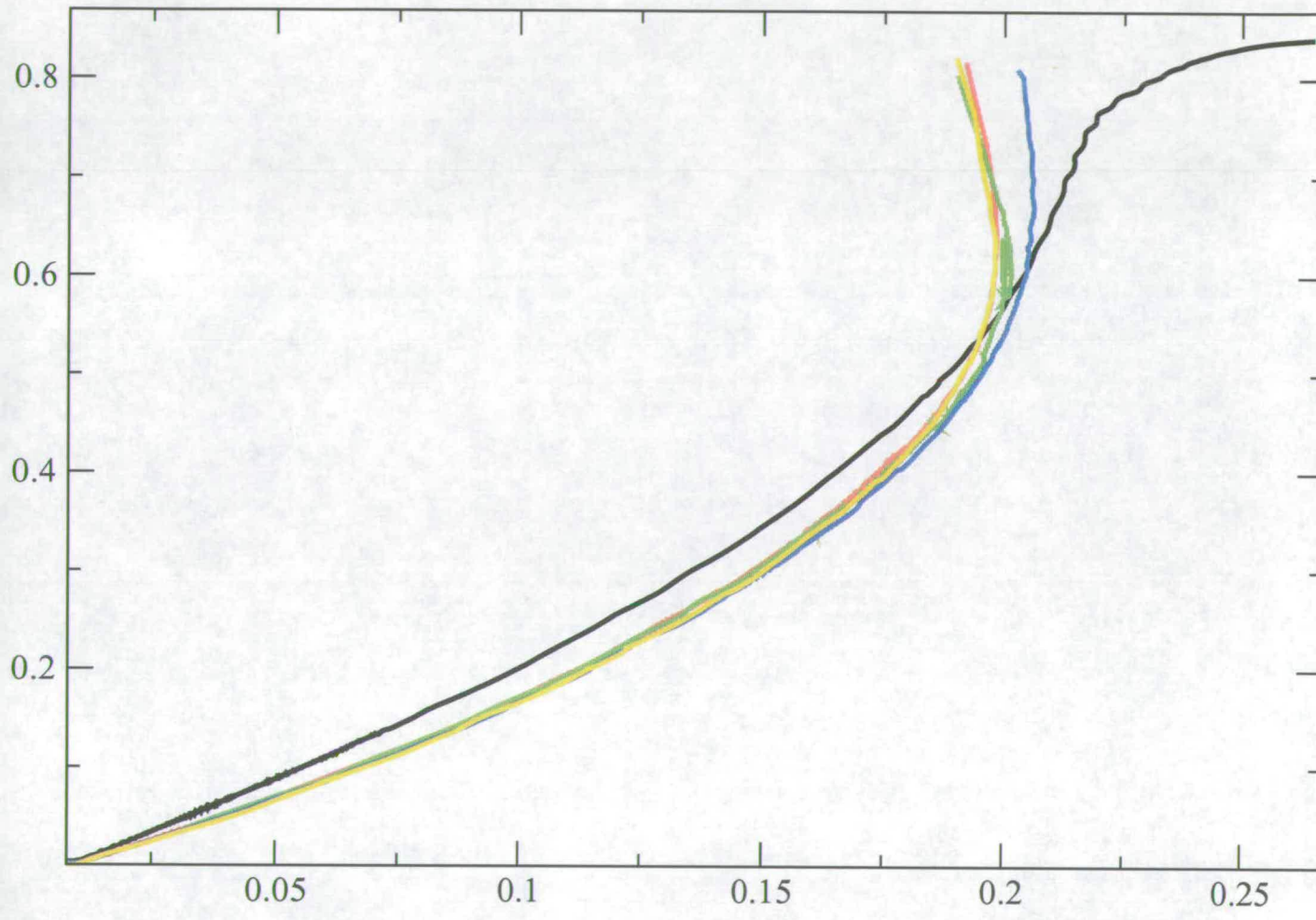

Figure 6.15: Effects of lattice size tested on smaller lattice on D vs Ca. For parameters see figure 6.14

runs using identical parameter sets with viscosity $\nu = 0.167$. It is certain that both these morphologies are unstable and that the shear step could not be refined sufficiently. However there is no significant difference in shape at the point of breakup. Looking at the Reynolds number vs capillary number plots (fig. 6.17) for these shows that the two lattice sizes converge well up until a capillary number of Ca= 0.15; thereafter the 40×200 plot continues at a lower gradient. Due to the bigger system size this deviation is thought to be caused by diffusion (see section 5.1.2).

From the results above the smallest acceptable size for the smaller lattice was chosen to be 60×100. This suggested that a larger size of 120×200 be appropriate, however 120×400 was chosen in order to accomodate the more elongated structures anticipated.

Using the highest viscosity simulated $\nu = 0.8768$ which will therefore produce the most elongated structures, the maximum error due to the periodic neighbour was estimated. By comparing the Reynolds number vs capillary number plots for system sizes 120×400 (black plot) and 120×600 (blue plot) (fig 6.18) an estimate on accuracy is found to be $\leq 10\%$ on this plot. This discrepency could be due to the influence of the flow field from the periodic neighbour, which would be expected to be relatively low due to the drop orientation almost along the undisturbed flow, but is most likely to be due to diffusion and tip streaming in these very elongated structures. Included in figure 6.18 are plots of the same test done using the lowest viscosity in our range. These form two lobed structures at the point where they become unstable and breakup (see fig 6.2). Although there is some divergence in the plots this is minimal and does not occur until the end stages of the process. It is thought that in this case although diffusion will be lower than in the more elongated structures they may be more susceptible to the hydrodynamic flow field of its periodic neighbour (which falls off as $\frac{1}{r}$) due to their orientation being $\sim 25^{o}$ to the undisturbed flow (opposed to nearly aligned with it, in the more elongated structures).

However the most surprising thing about this plot is that the gradient of the curve for the larger system size gradually increases rather than decrease as has been seen previously in the smaller lattices (see section 6.6).

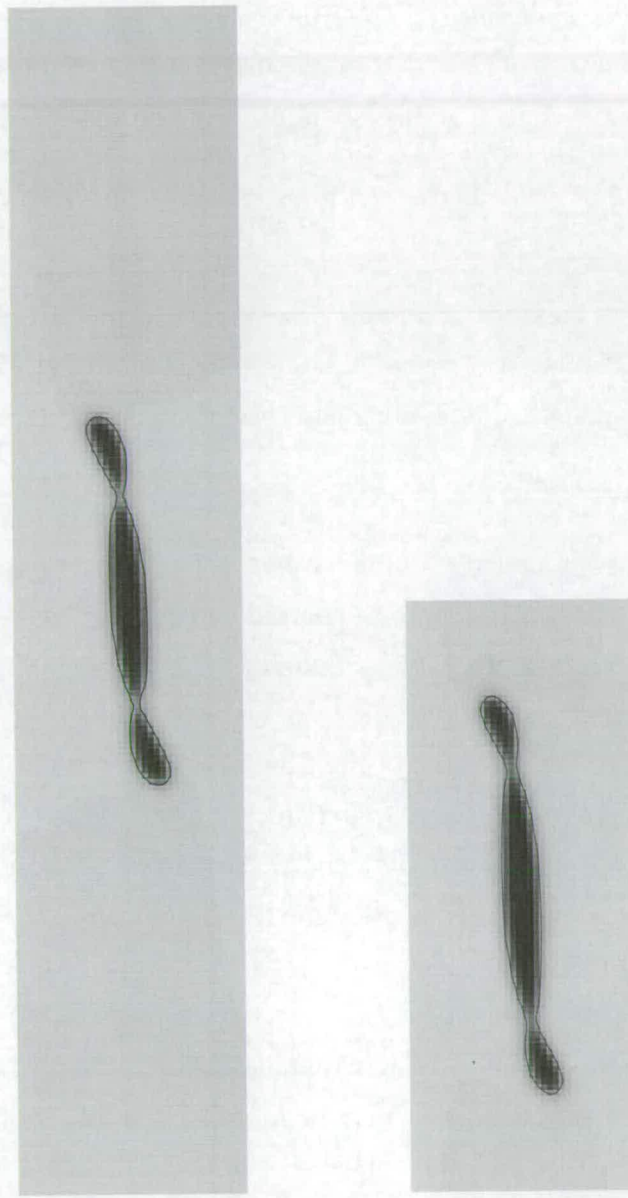

Figure 6.16: Effects of lattice size. RHS lattice has dimensions 40×200 final shear rate $\dot{\gamma} = 0.0102$ while the LHS lattice is 40×100 final shear rate $\dot{\gamma} = 0.0103$. Viscosity $\nu = 0.167$. Note these shapes are not stable.

runs using identical parameter sets with viscosity $\nu = 0.167$. It is certain that both these morphologies are unstable and that the shear step could not be refined sufficiently. However there is no significant difference in shape at the point of breakup. Looking at the Reynolds number vs capillary number plots (fig. 6.17) for these shows that the two lattice sizes converge well up until a capillary number of Ca= 0.15; thereafter the 40×200 plot continues at a lower gradient. Due to the bigger system size this deviation is thought to be caused by diffusion (see section 5.1.2).

From the results above the smallest acceptable size for the smaller lattice was chosen to be 60×100. This suggested that a larger size of 120×200 be appropriate, however 120×400 was chosen in order to accomodate the more elongated structures anticipated.

Using the highest viscosity simulated $\nu = 0.8768$ which will therefore produce the most elongated structures, the maximum error due to the periodic neighbour was estimated. By comparing the Reynolds number vs capillary number plots for system sizes 120×400 (black plot) and 120×600 (blue plot) (fig 6.18) an estimate on accuracy is found to be $\leq 10\%$ on this plot. This discrepency could be due to the influence of the flow field from the periodic neighbour, which would be expected to be relatively low due to the drop orientation almost along the undisturbed flow, but is most likely to be due to diffusion and tip streaming in these very elongated structures. Included in figure 6.18 are plots of the same test done using the lowest viscosity in our range. These form two lobed structures at the point where they become unstable and breakup (see fig 6.2). Although there is some divergence in the plots this is minimal and does not occur until the end stages of the process. It is thought that in this case although diffusion will be lower than in the more elongated structures they may be more susceptible to the hydrodynamic flow field of its periodic neighbour (which falls off as $\frac{1}{r}$) due to their orientation being $\sim 25^{o}$ to the undisturbed flow (opposed to nearly aligned with it, in the more elongated structures).

However the most surprising thing about this plot is that the gradient of the curve for the larger system size gradually increases rather than decrease as has been seen previously in the smaller lattices (see section 6.6).

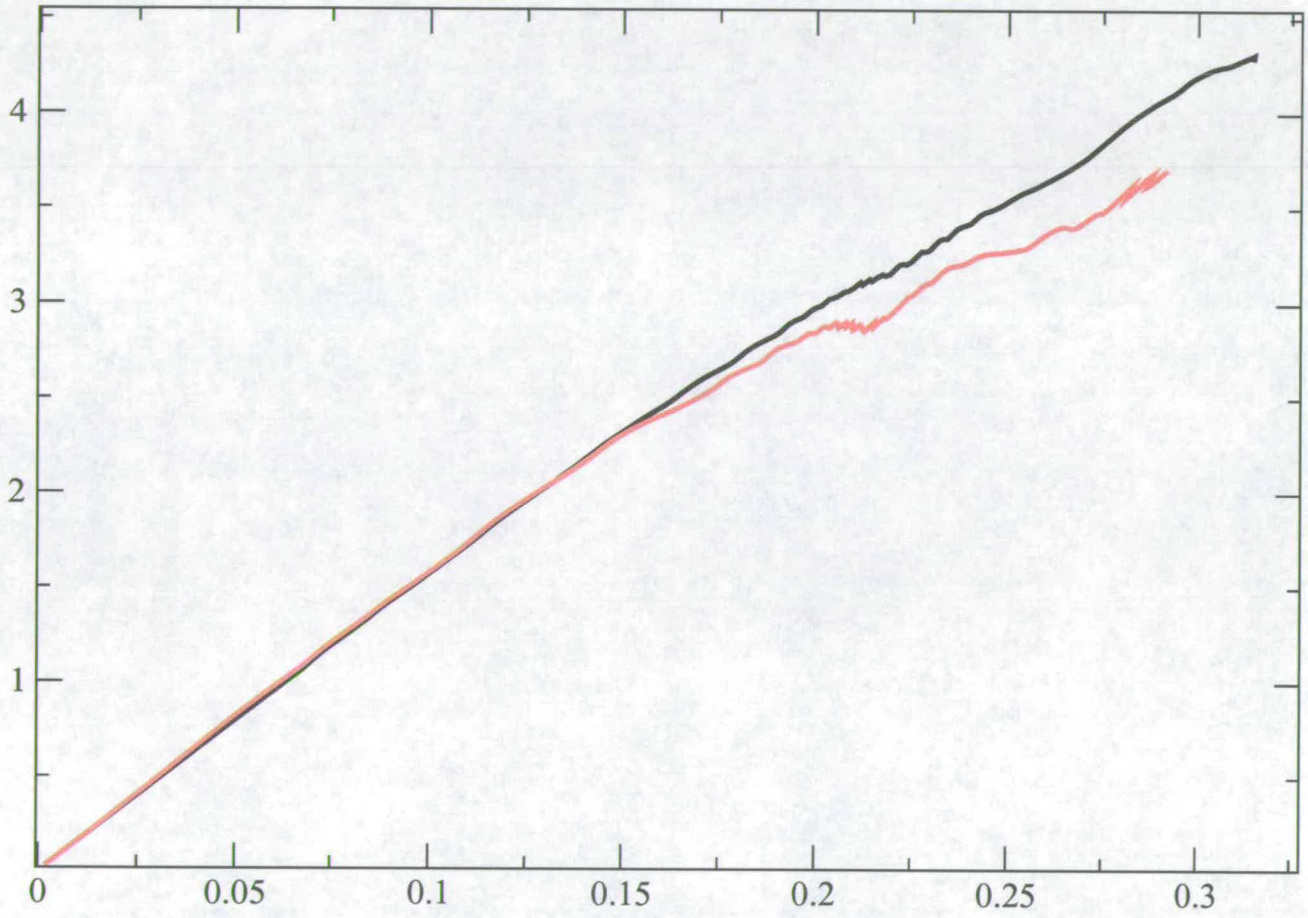

Figure 6.17: Re vs Ca for lattice sizes 40×200 (red plot) and 40×100 (black plot). Morphologies shown in previous plot.

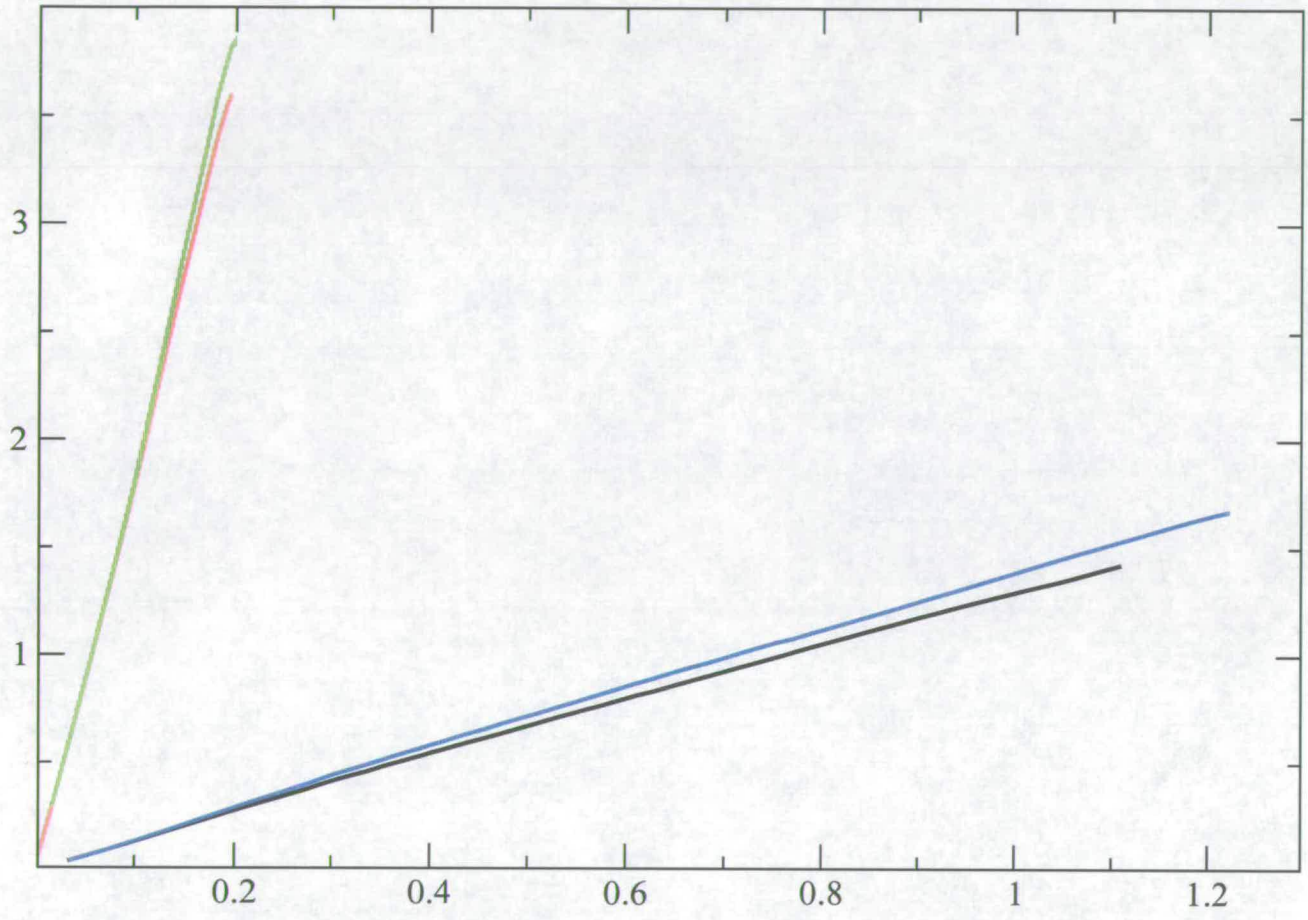

Figure 6.18: Re vs Ca for lattice sizes 120×400: $\nu = 0.2362$ (red plot), $\nu = 0.8768$ (black plot) and 120×600: $\nu = 0.2362$ (green plot), $\nu = 0.8768$ (blue plot). Shear rate increment $\Delta\dot{\gamma} = 1.67x10^{-4}$.

6.5.2 Tests on ramp methods

Effects of varying the size of the shear increment for a system undergoing fast (or unrestricted) ramps as defined in section 4.3 are investigated here. Identical parameter sets are used for the following simulations: surface tension $\sigma = 0.0456$, viscosity $\eta = 0.167$, mobility $M = 3.0$. Taking firstly the deformation with time graphs (fig 6.19), the black plot correspond to a lattice size of 40×100 with a shear step of 2.5×10^{-4}, the red plot corresponds to a lattice size of 40×100 with shear step 2.5×10^{-5}. Each plot reaches roughly the same deformation, and the run with the biggest shear step finishes much more rapidly. Now taking the deformation against capillary number (fig 6.20) it can be seen than the plots are almost convergent. An additional plot (blue) is included here corresponding to a lattice size of 40×100 which has been ramped 'continuously' (i.e. every time step) with a shear step of the order 10^{-9} (see section 6.5.1 and 4.3). This run ends sooner than the others which could be attributed to the ramp mechanism being slower and more sensitive as to where the breakup happens. The red and black plots representing a lattice size of 40×100 with shear rates of 2.5×10^{-4} and 2.5×10^{-5} respectively, are almost identical showing that to this accuracy the difference in shear step has little effect on the outcome.

Looking at the Reynolds number against capillary number plot (fig 6.21) the results of the different ramping methods are seen to converge well, concurring with the deformation against capillary number plots. This graph shows again that the continuous ramp finishes sooner which as mentioned above may attest to its increased sensitivity, however up until this point it agreed well with the stepped ramp.

From above it can be seen that the size of the ramp step has little effect on the end results; the important thing is that the drop be allowed to reach equilibrium at the new shear rate before ramping further. Comparison of results with a continuous ramp and a stepped ramp also give good convergence however these do suggest that the continuous ramp, with a sufficiently smaller ramp step, is more sensitive to determine the point of breakup. Care must therefore be taken with the stepped ramp to ensure the step is refined sufficiently. This has been done in the work reported in previous sections.

6.6 Wall effects

It seems certain that the walls play a large role in the characteristics of breakup. Fluid flow generated by the interface due to an increase in shear is conjectured to perhaps impinge on the walls and cause the drop to rotate towards the flow lines more effectively in the higher viscosity cases. A possible explanation of the observed behaviour – where in the case of the restricted ramp (or slow ramp, see 6.1) the lower viscosity simulations assume a final stable two lobed morphology aligned at an angle of $\sim 25^{\circ}$ to the undisturbed flow lines before breaking into two whereas the higher viscosity runs assume a final three lobed stable structure which is almost aligned with the flow (experiencing a minimum of shear stress) – could be the Bernoulli force.

In the most inviscid cases the higher shear rate needed to produce deformation could create a lower pressure region next to the walls near the tips of the drop, having the effect of 'sucking' the drop towards the walls increasing the shear stress on it. This effect is also described by Renardy and Cristini 2001 [16] as a mechanism for breakup in systems dominated by inertia. The findings of Sheth and Pozrikidis 1995 [19] are also worth noting in conjuction with the above. They look at the structure of the flow field as the Reynolds number is increased via the vorticity field, shear stress at walls and drag force distribution along the walls. They conclude that the maximum vorticity grows and becomes fixed at regions of maximum interfacial curvature, the maximum shear stress shifts from midway between a drop and its periodic neighbour towards the centre of the drop, and the drag force along the walls decreases. How these vary with wall width would also be worth studying.

Two final tests of the wall effects were made using the slow or restricted ramping method (see section 4.3). Choosing the largest viscosity $\nu = 0.8768$ in the range simulated in order to reach the shear rates necessary, the simulation was rerun with all other parameters kept as before except the lattice size: a 'wider' lattice size of 200×400 was selected. Comparing the resulting final configurations from this and the original lattice size 120×400 (fig 6.22a and b, 6.24 and 6.25) gives two very different outcomes. As a second check results from lattice sizes of 120×600 and 200×600 are included for comparison (see figures 6.22c, 6.22d and 6.26 and 6.27). These all confirm and are consistent with the previous tests made.

Shifting the solid walls further away has an effect analogous to increasing the viscosity at a constant lattice size; that is the resulting final structure is two lobed compared with three in the 'narrower' lattice.

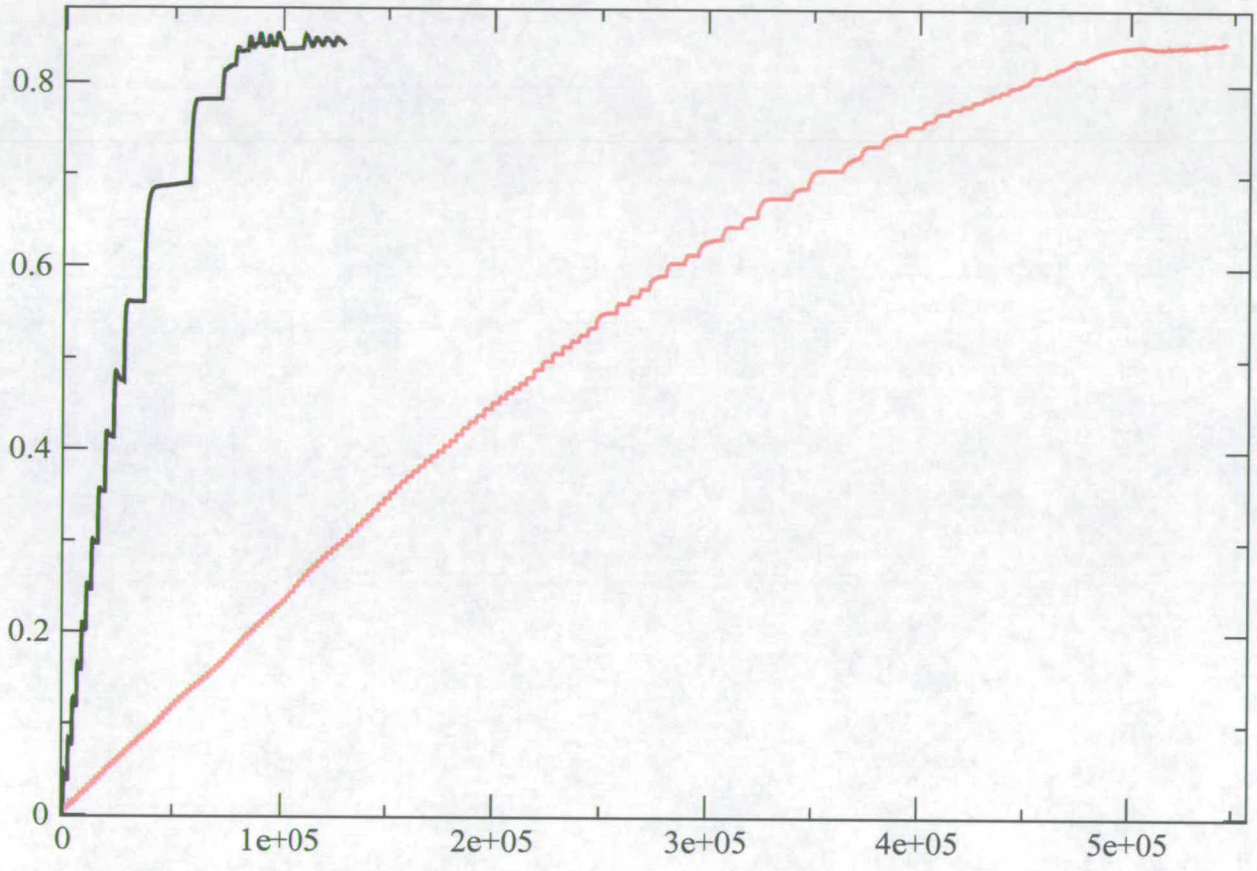

Figure 6.19: Effect of velocity ramp increment: deformation vs time. Lattice size 40 x 100 with velocity ramp increment $u_{wall} = 2.5x10^{-4}$ (black plot) and $u_{wall} = 2.5x10^{-5}$ (red plot).

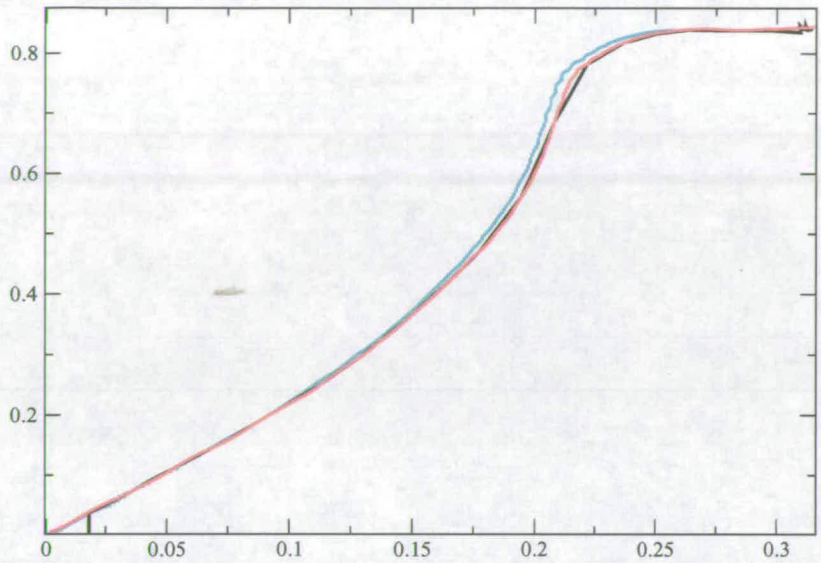

Figure 6.20: Effect of velocity ramp increment: D vs Ca. Blue plot shows a 'continuous' ramp for comparison. Other ramp step increments given in fig 6.19.

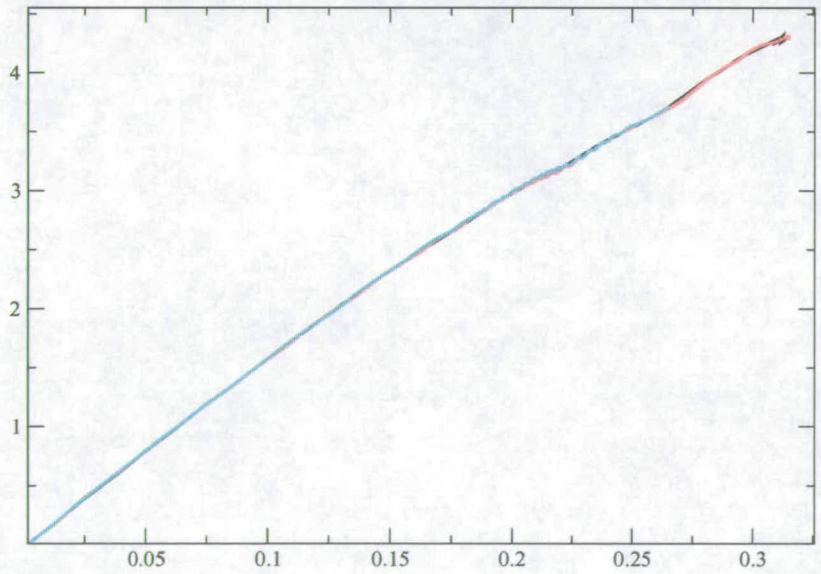

Figure 6.21: Effect of velocity ramp increment: Re vs Ca. See previous figures for details.

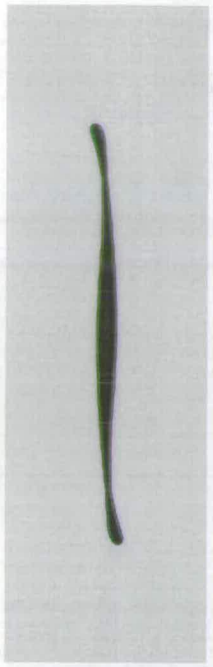

a) Final config. for lattice size 120×400

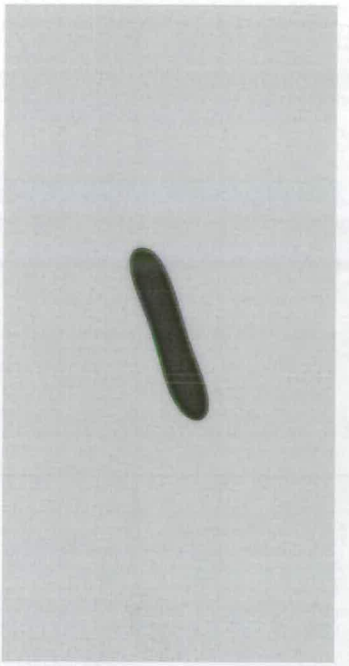

b) Final config. for lattice size 200×400

c) Final config. for lattice size 120×600

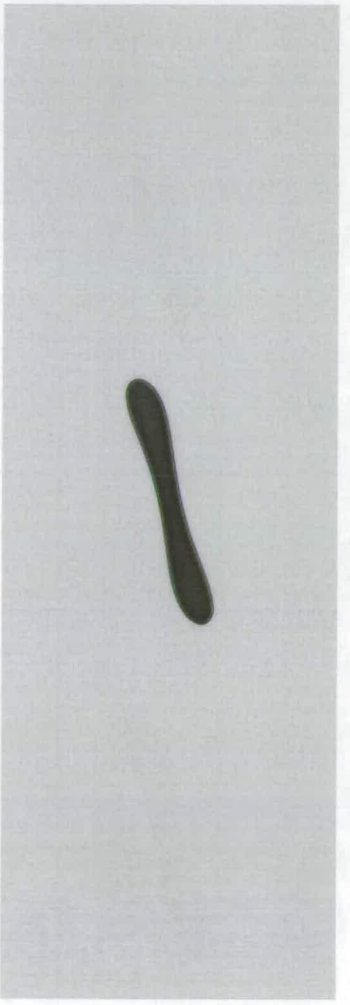

d) Final config. for lattice size 200×600

Figure 6.22: Importance of lattice size on final configuration

From the deformation vs capillary number curve (fig 6.24) the charateristic 'long tail' of the three lobed shape in the narrower 120×400 lattice contrasts with the constant upward curving of the two lobed shape in the wider 200×400 lattice. The Reynolds number vs capillary number (fig 6.25) highlights the difference in values of the parameters necessary for breakup under the restricted ramping conditions: a capillary number of ~ 0.35 is required for the wider lattice compared to ~ 1.1 in the narrower lattice. Evident here is that these larger lattices do not seem to experience the same amount of dissolution as in smaller lattices; the gradient of the (blue) plot for the 200×400 increases and does not decrease as was the case when testing the smaller lattice sizes (see section 6.5.1 figures 6.14 and 6.18). A hint as to what might be happening is given from the plot of the current drop radius against time (fig 6.23). It had been assumed that trends found for the smaller lattices would continue to larger lattice sizes; this however in the light of the above is not the case. Diffusion currents either due to the high mobility and/or combined with the offset of the order parameter to inhibit diffusion in the smaller lattice (section 5.2.4) now over compensate. Another possible factor is shape dependent diffusion; that is more elogated structures with regions of high curvature will suffer more diffusion and tip streaming.

Although it is unlikely that the configuration for the 120×400 and the 120×600 lattice (fig 6.22a and 6.22c) are stable, they suggest a shape like figure 6.1h just before breakup; if so the two very different morphologies at the point of break up can only be attributed to the proximity of the walls. (The morphology in fig 6.22d is also expected to be unstable and a stable shape akin to fig 6.22b is likely.)

Velocity fields generated by the interface may impinge on the walls and push or squeeze the drop towards the centre line. In relatively inviscid flows any flow perturbation or vorticity created and interacting with the walls could be carried down stream so that it cannot influence the breakup mechanics; wider walls may also facilitate this.

The effect of increasing the viscosity for a restricted or slow ramped case can be reproduced by decreasing the width of the solid walls of the simulation (all other parameters including viscosity kept constant). In other words the effect of increasing viscosity can be delayed by widening the solid walls. What is certain is that the proximity of the walls combined with an increase in viscosity over a threshold value inhibits droplet breakup.

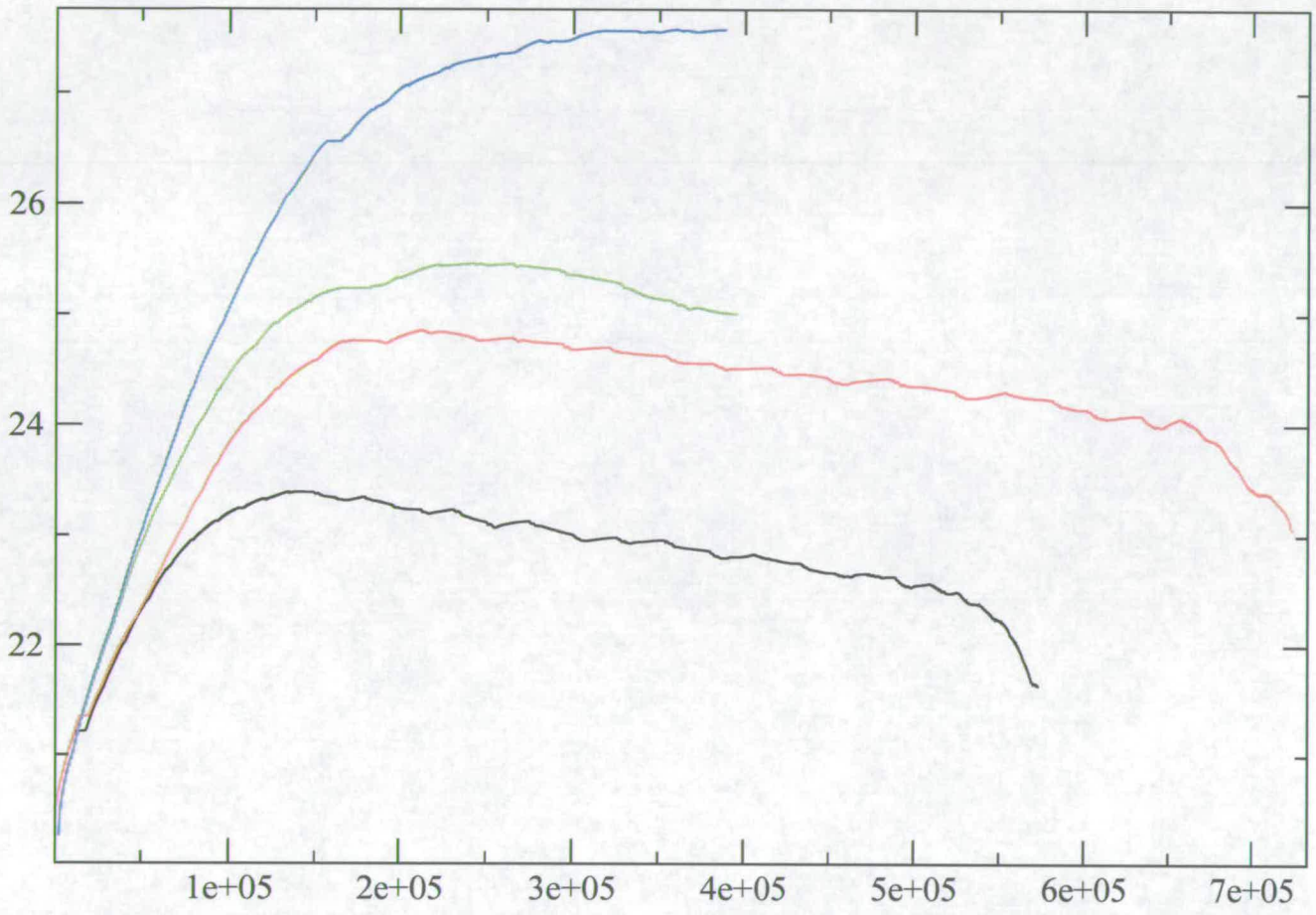

Figure 6.23: radius vs time plots for lattice sizes (blue) 200x600, (black) 120x400, (red) 120x600, (green) 200x400 for $\nu = 0.8768$

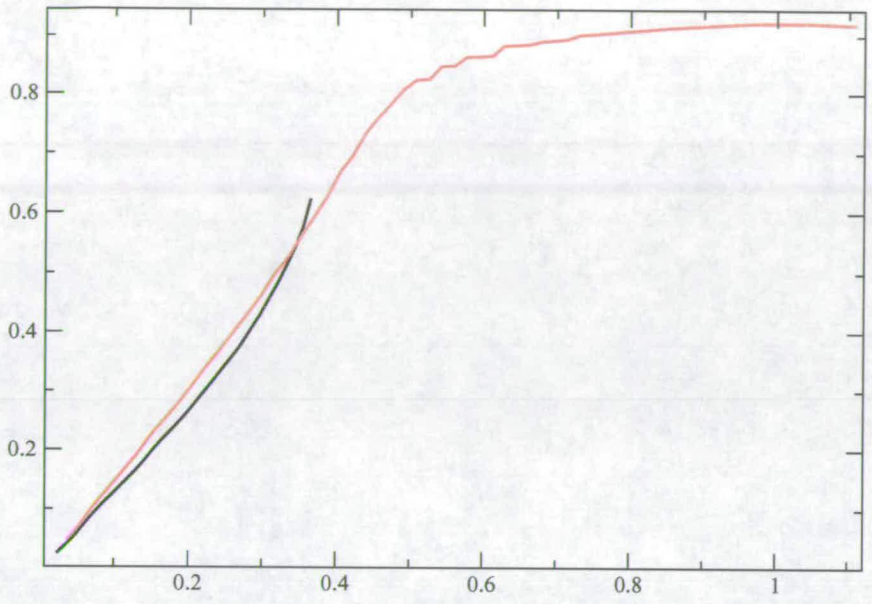

Figure 6.24: D vs Ca plots for lattice sizes (black) 200x400 and (red) 120x400 for $\nu = 0.8768$

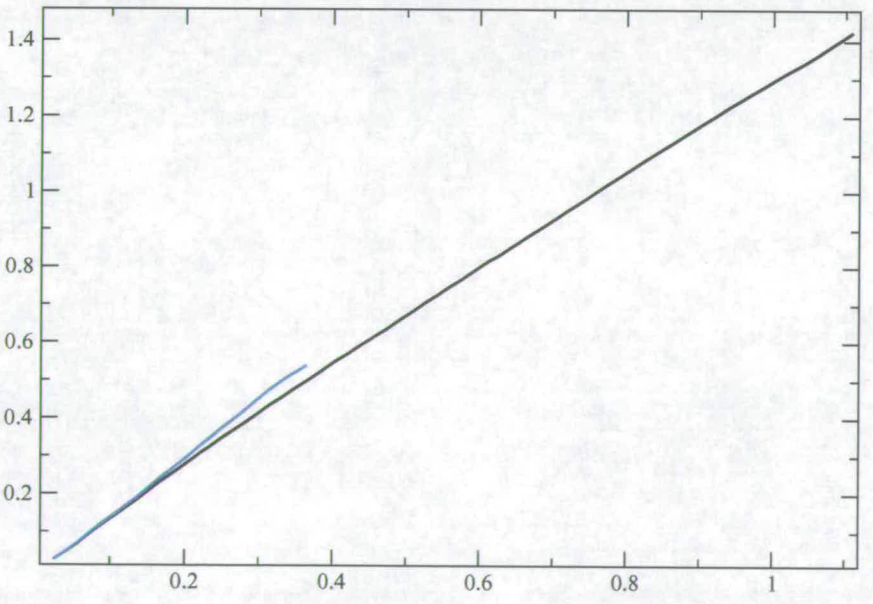

Figure 6.25: Re vs Ca plots for lattice sizes (blue) 200x400 and (black) 120x400 for $\nu = 0.8768$

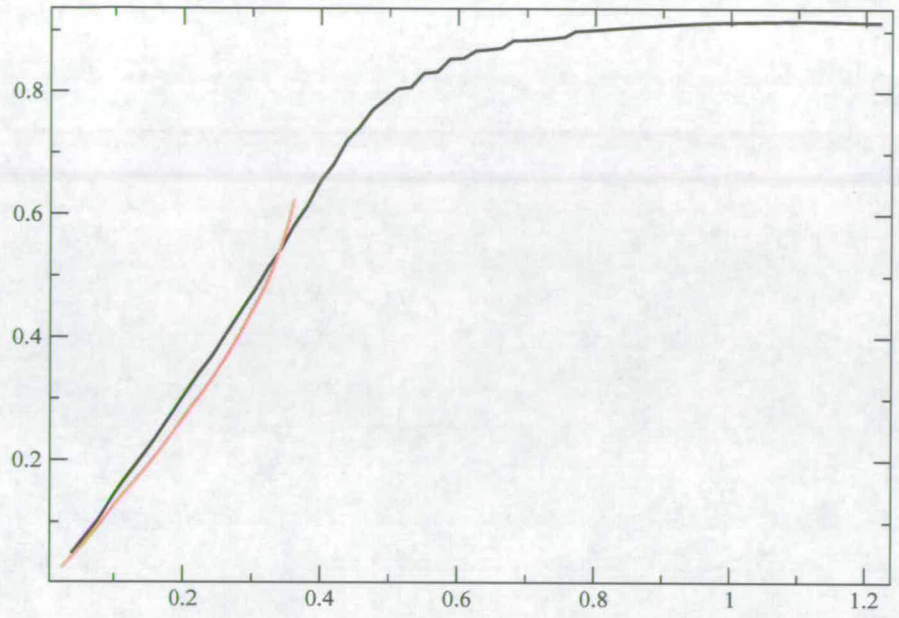

Figure 6.26: D vs Ca plots for lattice sizes (black) 120x600 and (red) 200x600 for $\nu = 0.8768$

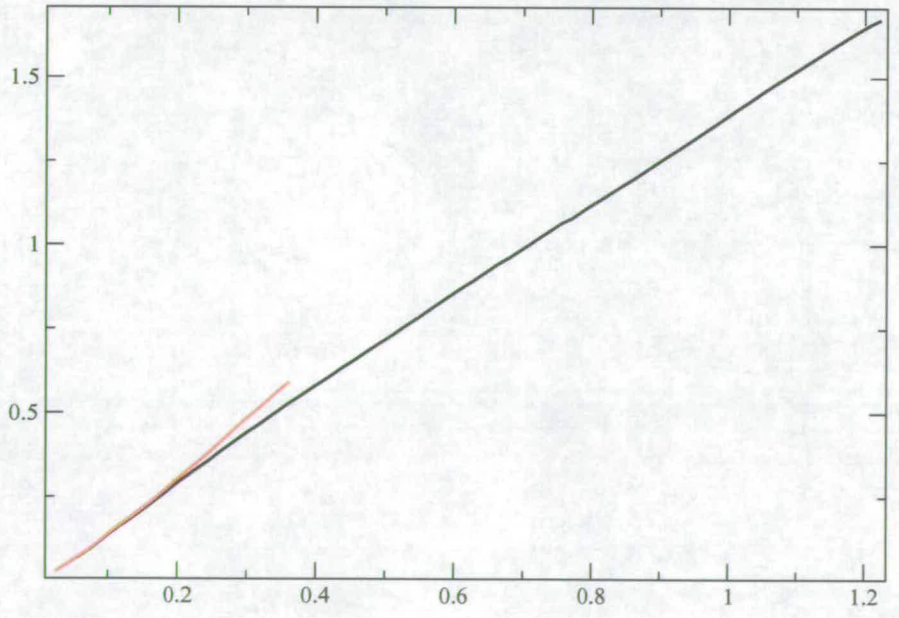

Figure 6.27: Re vs Ca plots for lattice sizes (black) 120x600 and (red) 200x600 for $\nu = 0.8768$

Chapter 7

Comments and Conclusions

From the findings here it would seem that for any hydrodynamic (non diffusive) breakup to occur in two dimensions a non-zero Reynolds number is required. For the lattice size used here, as the viscosity is increased (Reynolds number decreased) so the deformation and capillary number necessary for breakup increases (see figs. 6.7.and 6.8). The limiting case of Stokes flow is simulated (section 6.3) under the same criteria as for a restricted ramp (section 4.3) and the deformation vs capillary number is given in figure 6.12. The elongated structures also reach a limit in this case and the final morphology of the Stokes flow run is shown in figure 6.13. This extremely elongated shape is only 5-6 lattice units in width with little curvature exhibited along its sides. It is expected that this structure would continue elongating until it finally reached a point where the interfaces would get sufficiently close that diffusion would become dominant and lead to the drop dissolving.

Prior to breakup in three dimensions the final deformation reached is anticipated to be smaller than those found here in two dimensions. Breakup would be instigated at lower deformations due to the second radius of curvature and the additional Laplace pressure resulting from it. However it would be necessary to conduct a similar study in three dimensions before this could be firmly concluded. For the case of negligible inertial forces in three dimensions previous studies [13] give a critical deformation of $D \sim 0.55$ at breakup from a numerical simulation and one of $D \sim 0.6$ is obtained in experiments by Rumscheidt and Mason (1961). This may be in accordance with the lower end of the range of viscosities simulated here (see fig 6.2 and fig 6.7) however it does not agree with the higher end and is indeed very different from the limiting

case of Stokes flow mentioned above. So whilst the main instigating mechanisms of breakup in three dimensions are hydrodynamic this may not be the case in two dimensions.

A very important role in the characteristics of drop breakup is played by the system size. Lattices of larger dimensions will lead to a greater diffusion of material from the drop (see 5.2.4). This can be accounted for in the results by ensuring that the measure of drop radius used in calculations is derived from the drop volume at each sample point. However if the lattice size is too large diffusion will dominate and interfere with the breakup process; these cases are easily spotted from the data as a marked downturn in the Re vs Ca plots (see fig 6.14). Non constant drop volume may also be due to tip streaming (see section 5.2.5) where material is eroded from the drop tips by the shear flow or to shape dependant diffusion which will be most apparent in elongated structures with areas of high curvature. To counteract this requires careful consideration of the mobility parameter.

The influence on the breakup process of the periodic neighbouring drop is due to its flow field impinging on its neighbour and is thought to be more significant in the two lobed break up where the droplet is at an angle to the undisturbed flow (see 6.5.1). An extremely important role on this process is played by the solid walls of the simulation lattice. Section 6.6 details a simulation for viscosity $\nu = 0.8768$, repeated with identical parameters however with a lattice size of 200×400. The previous run used a lattice size of 120×400 and produced a three lobed final structure however this time the structure at the point of breakup is one of two lobes. Figures 6.24 and 6.25 (see also figs 6.26 and 6.27) give the plots of deformation vs capillary number and Reynolds number vs capillary number respectively and are evidence of the very different behaviour: a final three lobed configuration resulting from the 120×400 lattice is now two lobed when the run is conducted in a wider lattice 200×400.

Using a constant lattice size of 120×400 with all other parameters identical but varying the viscosity a similarly sharp contrast in behaviour of the drop as it is taken to the point before breakup is exhibited when it undergoes slow (or restricted) ramping (6.1). The Reynolds number vs capillary plot for this situation (fig 6.8) demonstrates where the final stable shape of the drops change from two lobed to three lobed.

The interplay of solid walls and the inertia of the fluid flow gives rise to the change in behaviour in droplet breakup.

Renardy and Cristini (2001) [16] have observed an effect akin to aerodynamic lift in three

dimensional simulations of inertia influenced breakup. It may be that the Bernoulli force is causing a similar difference in behaviour here.

What is also done in this work [16] that would be interesting to look at here is the 'inertia-induced wobbling' which may be similar to the overshoot seen in the deformation against time plots of the most inertial runs. To model this they use a simple equation describing the motion of a mass-spring system,

$$m\ddot{x}(t) + c\dot{x}(t) + \sigma x(t) = 0 \tag{7.1}$$

where the mass is given by $m = \rho(4/3)\pi a^3$, the friction coefficient c, by the Stokes drag on a sphere, $c = 6\pi\mu a$ and the restoring force by the surface tension σ. Whether oscillations like these could contribute to the development of vortices (see figs. 6.4 and 6.6) (or perhaps vice versa) or are even implicated in destabilising a drop near criticality and causing pinch off is a matter for further work.

It would also be potentially illuminating to look at the structure and behaviour of the vorticity field, shear stress distribution and drag force on the simulation walls as some insight into how the walls affect the overall process might be gained. This has been carried out by Sheth and Pozridkidis [19] in their investigation into inertial effects on deformation of simply sheared drops.

The presence of vortices may influence and promote the breakup dynamics and may contribute to the difference in behaviour from (relatively) low to high Reynolds number simulations. Their existence can be verified by examining the velocity maps, in particular figures 6.4 and 6.6, which show the central region of an elliptical structure for viscosity $\mu = 0.181$. Here the tips of two vortical swirls can clearly be seen.

From the difference in the modes of breakup between the restricted and unrestricted ramping methods (sections 6.1 and 6.2) the importance of the flow history is clear. However, the main and perhaps the most interesting result of this study is as summerised in figure 6.8 – how varying the viscosity over a threshold value for a given lattice size leads to a sudden transition in the morphology of the last stable droplet under slow ramping of shear rate.

Bibliography

[1] B. J. Bentley and L. G. Leal. An experimental investigation of drop deformation and breakup in steady two dimensional linear flows. *J. Fluid Mech.*, 167:241–283, 1986.

[2] P. L. Bhatnagar, E. P. Gross, and M. Krook. A model for collision processes in gases. I. small amplitude processes in charged and neutral one-component systems. *Phys. Rev.*, 94:511, 1954.

[3] A. J. Bray. Theory of phase–ordering kinetics. *Adv. Phys.*, 43:357, 1994.

[4] S. Chen and G. D. Doolen. Lattice Boltzmann method for fluid flows. *Ann. Rev. Fluid Mech.*, 30:329–64, 1998.

[5] J. C. Desplat, I. Pagonabarraga, and P. Bladon. LUDWIG: A parallel Lattice-Boltzmann code for complex fluids. *Comput. Phys. Commun.*, 134(3):273–290, 2001.

[6] J. Eggers. Theory of drop formation. *Phys. Fluids*, 7:941–953, 1995.

[7] A. Frischknecht. Effect of shear flow on the stability of domains in two dimensional phase separating binary fluids. *Phys. Rev. E*, 56:6970–6980, 1997.

[8] I. Halliday, C. M. Care, S. Thompson, and D. White. Induced burst of fluid drops in a two-component lattice Bhatnager-Gross-Krook fluid. *Phys. Rev. E*, 54:2573–2576, 1996.

[9] V. M. Kendon. *Finite Reynolds number effects in fluid mixtures: an investigation using numerical simulation methods.* PhD thesis, University of Edinburgh, 1999.

[10] V. M. Kendon, M. E. Cates, I. Pagonabarraga, J.-C. Desplat, and P. Bladon. Inertial effects in three-dimensional spinodal decomposition of a symmetric binary fluid mixture: a lattice Boltzmann study. *J. Fluid Mech.*, 440:147–203, 2000.

[11] A. J. C. Ladd. Numerical simulations of particulate suspensions via a discretized Boltzmann equation. Part 1. Theoretical foundation. *J. Fluid Mech.*, 271:258, 1994.

[12] J. Plateau. *Acad. Sci. Bruxelles Mem.*, 23:5, 1849.

[13] J. M. Rallison. A numerical study of the deformation and burst of a viscous drop in general shear flows. *J. Fluid Mech.*, 109:465–482, 1981.

[14] J. M. Rallison. The deformation of small viscous drops and bubbles in shear flows. *Ann. Rev. Fluid Mech.*, 16:45–66, 1984.

[15] Lord J. W. S. Rayleigh. *Proc. London Math. Soc.*, 10:4, 1879.

[16] Y. Y. Renardy and V. Cristini. Effect of inertia on drop breakup under shear. *Phys. Fluids*, 13(1):7–13, 2001.

[17] Y. Y. Renardy and V. Cristini. Scalings for fragments produced from drop breakup in shear flow with inertia. *Phys. Fluids*, 13(8):2161–2164, 2001.

[18] F. Savart. *Annal. Chim*, 53:337, 1833.

[19] K. S. Sheth and C. Pozrikidis. Effects of inertia on the deformation of liquid drops in simple shear flow. *Computers and Fluids*, 24(2):101–119, 1995.

[20] E. D. Siggia. Late stages of spinodal decomposition in binary mixtures. *Phys. Rev. A*, 20(2):595–605, 1979.

[21] H. A. Stone. Dynamics of drop deformation and breakup in viscous fluids. *Ann. Rev. Fluid Mech.*, 26:65–102, 1994.

[22] M. R. Swift, E. Orlandi, W. R. Osborn, and J. Yeomans. Lattice Boltzmann simulations of liquid-gas and binary fluid systems. *Phys. Rev. E*, 54:5041, 1996.

[23] G. I. Taylor. The viscosity of a fluid containing small drops of another fluid. *Proc. Roy. Soc. A*, 138:41, 1932.

[24] G. I. Taylor. The formation of emulsions in definable fields of flow. *Proc. Roy. Soc. A*, 146:501, 1934.

[25] A. J. Wagner and I Pagonabarraga. Lees-edwards boundary conditions for lattice Boltzmann. *J. Stat. Phys.*, 107(1-2):521–537, 2002.

[26] Alexander J. Wagner and J. M. Yeomans. Effect of shear on droplets in a binary mixture. *International Journal of Modern Physics C*, 8(4):773–782, 1997.

[27] H. Xi and C. Duncan. Lattice Boltzmann simulations of three dimensional single droplet deformation and breakup under simple shear flow. *Phys. Rev. E*, 59:3022, 1999.